

Coriolis force effect in steady and unsteady flow characteristics with convective heat transfer through a curved square duct

Mohammad Sanjeed Hasan¹, Rabindra Nath Mondal² and Giulio Lorenzini^{3*}

¹Department of Mathematics, Bangabandhu Sheikh Mujibur Rahman Science and Technology University, Gopalganj-8100, Bangladesh

²Department of Mathematics, Jagannath University, Dhaka-1100, Bangladesh

³Department of Engineering and Architecture, University of Parma, Parma 43124, Italy

ABSTRACT: The uses of curved ducts are applied not only to omnipresent the engineering machinery but also to the human body. Therefore, scholars so much are interested in investigating the phenomenon of flow through different types of ducts for the benefit of mankind. To the author knowledge, there is no known detailed study about the change of fluid flow behavior for both positive and negative rotation through the curved square duct. In the ongoing exploration, various types of fluid phenomena such as solution structures, time-history analysis, and temperature gradients have been performed for an extensive range of rotational parameters, the Taylor number, Ta . The solution structures have been enumerated by the spectral method whereas the time history analysis has been calculated by the function collocation as well as the Crank-Nicolson together with Adam-Bashforth method. It has seen that different types of flow instabilities have been found from the steady and unsteady solution. Two types of flow velocity, axial and secondary flow, and their temperature profiles have been also explored for different rotational parameters. The steady solutions have shown that the flow patterns have a significant change at their turning points. In the time history analysis, especially four types of flow characteristics, steady-state, periodic, multi-periodic and chaotic oscillation has established, where only two vortexes secondary flows have been found for the steady-state solution and two to six vortex have been consisted for the regular and irregular oscillation. In this study, a sub-sequential connection between the axial flow, secondary flow, and the temperature profiles have been built up. Moreover, understanding more clearly about the regular and irregular oscillation, phase spaces and power spectrums have been also obtained. The analysis of heat transfer has shown that the heat is transmitted from fluid particles, as a result, convective heat transfer has occurred and the heat in the fluid has increased, consequently, the fluid has mixed and affected the vortex structures. It is noted that Code::Blocks is the secondary tool to collect the data and TECPLOT 7 is used for visualization of the data.

Keywords: Curved ducts, Steady solution branch, Linear stability, Time-history analysis, Vortex structures, Temperature Gradients.

1. INTRODUCTION

Research on flow through the ducts have not begun from today but has been going on for an era. It has a spacious application in mechanical and chemical engineering, such as rocket engine, gas turbines, chemical reactors, lubrication system, electric generators and also in biomedical engineering, for example, circulating tumor cells, lung, vein, arteries, microfiltration. Due to increasing the fluid flow investigation through ducts, nowadays new types of ducts are discovering. Contrariwise, the governing equation of the flow through the ducts contains various useful parameters, so most scholars have attracted to discuss the effects of flow structures for changing the parameters. There are numerous available articles on fluid flow through different ducts for various cross-sections. Some of them, Yanase et al. [1, 2] (square and rectangular duct), Rumsey et al. [3] (U-duct), Chandratilleke et al. [4] (rectangular and elliptical duct), Ahmadloo et al. [5]

(helical pipe), Garnier [6] may be mentioned for distinguished analyses. The fluid circumstance inside a curved duct attaches many significant phenomena such as bifurcation structure, unsteady solutions, flow velocity analysis, heat transfer, etc.

One of the mentionable subjects in curved ducts is to examine the bifurcated structure. By analyzing trapezoidal pipe flow, the bifurcation at the turbulent flow has been obtained by Canton et al. [7]. They have also taken a snapshot of a curved pipe and shown the limit points of the turbulent flow including the phase space and power spectrum density. Leong et al. [8] have provided a single bifurcation model which calculated particle image velocimetry measurements so that they have shown their results by experimentally. Vortical and bifurcation constitution through a cylinder has been established by Sau and Hsu [9] three-dimensionally. Lin et al. [10] have narrated the bifurcation for two-dimensional conducting fluid with including some magneto-hydrodynamic

* Corresponding Author: giulio.lorenzini@unipr.it

parameters. Bifurcation diagrams for both elliptical and rectangular ducts have been performed by Machane [11]. They have also computed the total turning paths with symmetry-breaking bifurcation for various aspect ratios. Very recently, three different types of bifurcation structures with their linear stability have been found by Ullah and Ali [12] for peristaltic transportation through the curved channel. Seven symmetric and four asymmetric solution branches for tightly coiled ducts have been gained by Liu and Wang [13]. They have also disclosed the structural change of bifurcation for changing the grid points. Chen et al. [14] tried to analyze the bifurcation structure for a small range of aspect ratio. They have also described the change of vortex structure at limit points of the curved rectangular duct. Almost the same study together with linear stability has been also conducted by Yanase et al. [15] for a wide range of aspect ratios. A complete study on bifurcation for non-rotating curved square ducts has been present by Mondal et al. [16] study. They have considered the spectral method to find out steady solution branches. Two types of bifurcation such as Holf and Pitchfork bifurcation has been acquired in their study. Centrifugal effects in bifurcation are another important objective in their study. By applying Homotopy perturbation and semi-analytical method, Nowruzi et al. [17] have exhibited the effects of aspect ratios and curvature in the critical points of bifurcation. Lin et al. [18] have executed the bifurcation structure for through the cylinder for strong rotational speed. They have also supported their findings with unsteady solutions.

It is almost well known to all that unsteady flow characteristics are widely audited in metallic industries, physiological flows, and human repertory system. Time-dependent solution with respect to the drag and lift coefficient for several Reynold numbers and gap spacing parameters across multiple staggered rows of cylinders have been explored by Nazeer et al. [19]. They have also validated their periodic oscillation by power spectrum analysis. Zhang et al. [20] have conducted almost the same study for four square cylinders where the cylinders have been kept at an equal distance from each other. Hashemi et al. [21] have measured the fluctuation of the velocity components regarding with time through the curved pipe. Two, as well as three-dimensional transitional behaviors for non-rotating curved duct, have been studied by Yanase et al. [22]. Arakeri et al. [23] have experimented the unsteady flow behaviors through a curved pipe for a large of Dean and Womersley numbers. Unsteady behaviors in a square enclosure where mixed convection happened have been steered out by Zhang et al. [24]. Dynamical responses of time evolution calculation at various Dean numbers have been also initiated by Wang and Yang [25] where they have also compared their numerical outcome with the experimental data. Transient behaviors in thermal analysis for large aspect ratios have been calculated by Arpino et al. [26]. Mondal et al. [27] have computed the change of unsteady flow behaviors in the cooling and heating

sidewalls for several Dean number, Grashof number and aspect ratio. They have also justified their oscillating flows by drawing the phase space analysis. Three types of flow oscillations such as steady-state, periodic, and chaotic have been established in the Hasan et al. [28] study flow for small curvature. Zohurul et al. [29] have considered the function collocation method of seeking out the unsteady solutions for both positive and negative rotation of the duct.

Flow visualization is another significant material for the duct because it recounts about the effects of fluid and heat transfer mixing. Before saying about the flow in the duct, it should be known that Dean [30] was the first who had derived the governing equations of curved ducts. He related that the two vortexes secondary flow has converted into the four vortexes at the limit points of the steady solution and these two vortexes are designated as the Dean vortex. He also demonstrated that there are three types of potency such as centrifugal force, Coriolis force, and body force worked in the fluid flow. Here, it is noted that the centrifugal and Coriolis force forces are influenced by the duct curvature and the rotation of the duct. Ozaki and Maekawa [31] have shown the curvature effects in the curved duct flows. Numerical and experimental flow and heat transfer through the rectangular and elliptical curved duct have been illustrated by Chandratilleke et al. [32]. Ferdows et al. [33] have explained the Dean number karma through the helical duct for different rotational numbers. Numerical investigation on the thermal buoyancy and the downward flow behavior of the power-law fluids has been simulated by Bouzit et al. [34]. They have also vindicated their numerical analysis with the experimental data. Bayat et al. [35] have developed a numerical and experimental model to demonstrate about the upshot of the curvature, kinematic viscosity for curved and spiral microchannel. Li et al. [36] have pursued the numerical study of two-dimensional flow behaviors for changing the curvature and aspect ratios of the duct. They have also shown the flow velocity with the three-dimensional contours of the secondary flow where the flow fields have been measured by using the particle image velocimetry. Razavi et al. [37] have performed flow structure, heat, and entropy transmission through a curved rotating duct where they have applying the second law of thermodynamics in their work. Watanabe and Yanase [38] have attempted to develop a three-dimensional model to visualize the flow structures. Hardling [39] have proposed the Rayleigh-Ritz method to manifest the Dean vortices through the curved duct. Nowruzi et al. [40] have used the energy gradient method to report the flow structure through the curved rectangular duct 120° inlet. Considering the perturbation method as the main tool, Norouzi and Biglari [41] have accomplished the formation of the secondary flow structures. They have also sketched the vector plot of the secondary flow.

Heat transfer through the ducts is broadly used in fluid mixing devices, heating, and cooling in evaporators,

thermal power plants, air-conditioning equipment, turbo-machinery, refrigerators, fusion reactors, radiators for space vehicles, combustion chambers, automobiles, etc. Sasmito et al. [42] have evaluated the enhancement of heat transfer for the nano-fluid particle in coiled ducts. The influence of centrifugal and hydrodynamic instability in the heat transfer for non-rotating duct has been attained by Hasan et al. [43]. Jing et al. [44] have explained the enhancement of heat transfer for the duct structure and the pyrolytic reaction. Norouzi et al. [45] recounted the elasticity of steam function and the heat transfer for rotating curved duct by adopting the FTCS finite difference method. Heat transfer in the cooled and heated sidewalls of the square duct has been plotted numerically by Mondal et al. [46]. They also imparted to a connection between the steady and unsteady flows. Later, Mondal et al. [47] have also executed the same study for large aspect ratio where they have represented the relationship between the fluid mixing and the heat transfer through the curved duct. Ghobadi and Muzychaka [48] have correlated the pressure drop, heat flux, and heat transfer through the circular duct both numerically and experimentally. Shahmardan et al. [49] have analytically solved the convective heat transfer for different aspect ratios under fixed heat flux. They have also calculated the non-dimensional Neumann problem and got the critical aspect ratio when seeking out the local and mean Nusselt number.

The existing article has highlighted on the exploration of the steady solution branches, Linear stability analysis, change unsteady flow structures, flow velocity and temperature components, Vortex structures of secondary flow, and heat transmission of the flow through the curved rotating duct.

2. GOVERNING EQUATIONS

The schematic representation of the duct and the derivation of governing equations of the present study have been discussed in this section. Flow behavior through the duct is considered laminar, the density of the fluid is constant and cylindrical coordinate system is assumed, i.e. (r, θ, y) . Let, v_x , v_θ , and v_y are the velocity components of r , θ , and y respectively. So the governing equations are as follows,

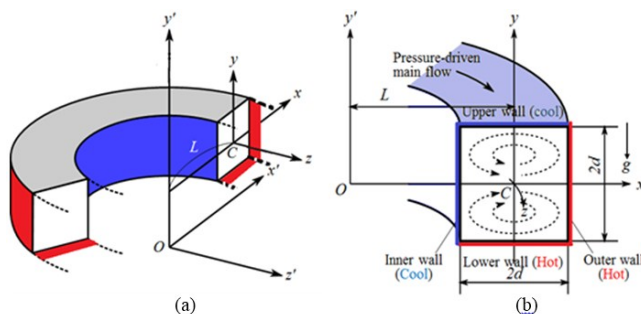


Figure 1: (a) The physical model of rotating curved square duct and (b) Cross-sectional view of the curved duct.

Continuity equation:

$$\frac{\partial v_r}{\partial r} + \frac{1}{r} \frac{\partial v_\theta}{\partial \theta} + \frac{\partial v_y}{\partial y} + \frac{v_r}{r} = 0 \quad (1)$$

Navier-Stokes equations:

$$\frac{\partial v_r}{\partial t} + (v \cdot \nabla) v_r - \frac{v_\theta^2}{r} = -\frac{1}{\rho} \frac{\partial P}{\partial r} + \nu \left(\tilde{\Delta} v_r - \frac{v_r}{r^2} - \frac{2}{r^2} \frac{\partial v_\theta}{\partial \theta} \right) \quad (2)$$

$$\frac{\partial v_\theta}{\partial t} + (v \cdot \nabla) v_\theta + \frac{v_r v_\theta}{r} = -\frac{1}{\rho r} \frac{\partial P}{\partial \theta} + \nu \left(\tilde{\Delta} v_\theta - \frac{v_\theta}{r^2} + \frac{2}{r^2} \frac{\partial v_r}{\partial \theta} \right) \quad (3)$$

$$\frac{\partial v_y}{\partial t} + (v \cdot \nabla) v_y = -\frac{1}{\rho} \frac{\partial P}{\partial y} + \nu \tilde{\Delta} v_y + \beta g T \quad (4)$$

Heat conduction equation:

$$\frac{\partial T}{\partial t} + (v \cdot \nabla) T = \kappa \tilde{\Delta} T \quad (5)$$

$$\text{Here, } v \cdot \nabla = v_r \frac{\partial}{\partial r} + \frac{v_\theta}{r} \frac{\partial}{\partial \theta} + v_y \frac{\partial}{\partial y}, \quad \tilde{\Delta} = \frac{\partial^2}{\partial r^2} + \frac{1}{r} \frac{\partial}{\partial r} + \frac{1}{r^2} \frac{\partial^2}{\partial \theta^2} + \frac{\partial^2}{\partial y^2}, \quad (6)$$

and the delegated notations ρ , ν , κ and g are the density, the kinematic viscosity, the coefficient of thermal conductivity and the gravitational acceleration respectively. To make the equation dimensionless, various type of parameters are used, such as L , the radius of curvature; d , the width and h , the height of the cross section. A necessary transformation has been considered for this investigation as follows:

$$r = L + dx', \quad y = hy', \quad L\theta = -dz', \quad T = T' \Delta T, \quad v_r = v_x = U_0 u', \quad v_y = v_z = U_0 v', \\ v_\theta = -v_z = U_0 w', \quad \rho = \rho_0 U_0^2 P', \quad G = -\frac{\partial P'}{\partial z'}, \quad \epsilon = \sqrt{\frac{2d}{L}} = \sqrt{2\delta}, \quad \delta = \frac{d}{L}, \quad l = \frac{h}{d}$$

Now some important parameters of the governing equations are described which can be implemented in many engineering areas. Such kind of parameter is G , is known as the pressure gradient which enumerates the rate of pressure with respect to the particular axis and other is δ , is also known as the curvature defined as the ratio between the width and the radius of curvature of the duct. It is evidently said that curvature plays a significant role in fluid related machinery. For example, Human veins are linked up with each other, as a result, various twisted ducts are constructed, and blood passes through the curved channel. For this, the governing equation presented in this paper can be also used in bio-engineering fields.

In addition, another parameter is l , is the aspect ratio of the duct, which is defined as the proportion of the height and width of the duct. It is used to understand whether the duct is square or rectangular. In the regarding paper, the cross section is square, i.e., the height and the width

are equal, so the height is replaced by width as also seen at the Figure 1. To calculate the governing equation numerically, aspect ratios are used in the numerical section which is termed as the truncation number.

However, as the paper focuses on two dimensional flow and the flow is uniform in z' direction, so $\frac{\partial}{\partial z'} = 0$

and $\frac{\partial p'}{\partial z'} = 0$. Now substituting the above assumption in equation (1) to (5), the transformed equations are,

Continuity equation:

$$\frac{\partial u'}{\partial x'} + \frac{\partial v'}{\partial y'} + \frac{\delta u'}{1 + \delta x'} + \frac{1}{1 + \delta x'} \frac{\partial w'}{\partial z'} = 0 \quad (6)$$

Navier-Stokes equations:

$$\frac{\partial u'}{\partial t'} + (v' \cdot \nabla') u' - \frac{1}{2} \epsilon^2 \frac{w'^2}{1 + \delta x'} = -\frac{\partial P'}{\partial x'} + \frac{\epsilon}{Dn} \left(\tilde{\Delta}_2 u' - \frac{\delta^2 u'}{(1 + \delta x')^2} \right) \quad (7)$$

$$\frac{\partial v'}{\partial t'} + (v' \cdot \nabla') v' = -\frac{\partial P'}{\partial y'} + \frac{\epsilon}{Dn} \tilde{\Delta}_2 v' + \frac{\beta g \Delta T l}{U_0^2} T' \quad (8)$$

$$\frac{\partial w'}{\partial t'} + (v' \cdot \nabla') w' + \frac{1}{2} \epsilon^2 \frac{u' w'}{1 + \delta x'} = -\frac{G}{1 + \delta x'} + \frac{\epsilon}{Dn} \left(\tilde{\Delta}_2 w' - \frac{\delta^2 u'}{(1 + \delta x')^2} \right) \quad (9)$$

Heat conduction equation:

$$\frac{\partial T'}{\partial t'} + (v' \cdot \nabla') T' = \frac{\kappa}{d U_0} \tilde{\Delta}_2 T' \quad (10)$$

Where, $(v' \cdot \nabla') = u' \frac{\partial}{\partial x'} + v' \frac{\partial}{\partial y'}$, and

$$\tilde{\Delta}_2 = \frac{\partial^2}{\partial x'^2} + \frac{\partial}{\partial y'^2} + \frac{\delta}{1 + \delta x'} \frac{\partial}{\partial x'}$$

Now, introducing the stream function and the vorticity vector, along x' and y' direction respectively,

$$u' = \frac{1}{1 + \delta x'} \frac{\partial \psi'}{\partial y'} \quad \text{and} \quad v' = -\frac{1}{1 + \delta x'} \frac{\partial \psi'}{\partial x'} \quad (11)$$

$$\Omega' = \frac{\partial v'}{\partial x'} - \frac{\partial u'}{\partial y'} = -\frac{1}{1 + \delta x'} \left(\frac{\partial^2}{\partial x'^2} + \frac{\partial^2}{\partial y'^2} - \frac{\delta}{1 + \delta x'} \frac{\partial}{\partial x'} \right) \quad (12)$$

Differentiating (8) and (9) with respect to x' and y' , and then subtract, we get the following equation

$$\frac{\partial \Omega'}{\partial t'} + \left(u' \frac{\partial}{\partial x'} + v' \frac{\partial}{\partial y'} \right) \Omega' - \frac{\delta u'}{1 + \delta x'} \Omega' + \frac{\epsilon^2 w'}{1 + \delta x'} \frac{\partial w'}{\partial y'} = \frac{\epsilon}{Dn} \left(\tilde{\Delta}_2 - \frac{\delta^2}{1 + \delta x'} \right) \Omega' + \frac{\beta g \Delta T l}{U_0^2} \frac{\partial T'}{\partial x'} \quad (13)$$

The simplified equations are found after removing the prime sign from the primitive equations as:

$$(1 + \delta x) \frac{\partial w}{\partial t} + \frac{1}{l} \frac{\partial (w, \psi)}{\partial (x, y)} - Dn + \frac{\delta^2 w}{1 + \delta x} = (1 + \delta x) \Delta_2 w - \frac{\delta}{l(1 + \delta x)} \frac{\partial \psi}{\partial y} w + \delta \frac{\partial w}{\partial x} - \delta Tr \frac{\partial \psi}{\partial y} \quad (14)$$

$$\left(\Delta_2 - \frac{\delta}{1 + \delta x} \frac{\partial}{\partial x} \right) \frac{\partial \psi}{\partial t} = -\frac{1}{l(1 + \delta x)} \frac{\partial (\Delta_2 \psi, \psi)}{\partial (x, y)} + \frac{\delta}{(1 + \delta x)^2} \left[3\delta \frac{\partial^2 \psi}{\partial x^2} - \frac{3\delta^2}{1 + \delta x} \frac{\partial \psi}{\partial x} \right] + \frac{\delta}{l(1 + \delta x)^2} \left[\frac{\partial \psi}{\partial y} \left(2\Delta_2 \psi - \frac{3\delta}{1 + \delta x} \frac{\partial \psi}{\partial x} + \frac{\partial^2 \psi}{\partial x^2} \right) - \frac{\partial \psi}{\partial x} \frac{\partial^2 \psi}{\partial x \partial y} \right] - \frac{2\delta}{1 + \delta x} \frac{\partial}{\partial x} \Delta_2 \psi + \frac{1}{l} w \frac{\partial w}{\partial y} + \Delta_2^2 \psi - Gr(1 + \delta x) \frac{\partial T}{\partial x} - Tr \frac{\partial w}{\partial y} \quad (15)$$

$$\frac{\partial T}{\partial t} + \frac{1}{l(1 + \delta x)} \frac{\partial (T, \psi)}{\partial (x, y)} = \frac{1}{Pr} \left(\Delta_2 T + \frac{\delta}{1 + \delta x} \frac{\partial T}{\partial x} \right) \quad (16)$$

Where, $\Delta_2 = \frac{\partial^2}{\partial x^2} + \frac{1}{l^2} \frac{\partial^2}{\partial y^2}$ and $\frac{\partial (f, g)}{\partial (x, y)} = \frac{\partial f}{\partial x} \frac{\partial g}{\partial y} - \frac{\partial f}{\partial y} \frac{\partial g}{\partial x}$

Governing equations (14) - (16) are invariant with respect to the $y = 0$. The non-dimensional parameters Dn , the Dean number, Gr , the Grashof number, and Pr , the Prandtl number are contained in equations (14) to (16), can be defined as,

$$Dn = \frac{Gd^3}{\mu\nu} \sqrt{\frac{2d}{L}} = \frac{Gd^3}{\mu\nu} \sqrt{2\delta}, \quad Gr = \frac{\beta g \Delta T d^3}{\nu^2}, \quad Tr = \frac{2\sqrt{2}\delta \Omega_r d^3}{\nu\delta}, \quad Pr = \frac{\nu}{\kappa}$$

In the proposed study, water is the main flow so the Prandtl number is specific, ($Pr = 7.0$); the Dean number and the Grashof numbers considered fixed, $Dn = 1000$ & $Gr = 100$; and the rotational parameter, Taylor number is varied within the range -2500 to 2500.

The given boundary conditions for axial (w) and secondary flows (ψ) are,

$$w(\pm 1, y) = w(x, \pm 1) = \psi(\pm 1, y) = \psi(x, \pm 1) = \frac{\partial \psi}{\partial x}(\pm 1, y) = \frac{\partial \psi}{\partial y}(x, \pm 1) = 0 \quad (17)$$

and also the boundary conditions for temperature (T) profiles are,

$$T(1, y) = y, \quad T(-1, y) = y, \quad T(x, 1) = x, \quad T(x, -1) = x \quad (18)$$

3. NUMERICAL CALCULATIONS

3.1 Process of numerical design

This section is formed on numerical calculation and in order to find out numerical calculation, spectral method is applied at the obtained non-dimensional zed momentum and energy equations. The key goal of this technique is the function expansion of the polynomial.

The required function is elaborated by the series which is also contained first kind Chebyshev polynomials of n^{th} order and explained as $C_n(x) = \cos(n \cos^{-1}(x))$. The functions expansion of $\varphi_n(x)$ and $\psi_n(x)$ are stated as

$$\left. \begin{aligned} \varphi_n(x) &= (1-x^2) C_n(x), \\ \psi_n(x) &= (1-x^2)^2 C_n(x) \end{aligned} \right\} \quad (19)$$

Furthermore, $w(x, y, t)$, $\psi(x, y, t)$ and $T(x, y, t)$ are expanded in terms of the expansion functions $\phi_n(x)$ and $\psi_n(x)$ as:

$$\left. \begin{aligned} w(x, y, t) &= \sum_{m=0}^M \sum_{n=0}^N w_{mn}(t) \phi_m(x) \phi_n(y) \\ \psi(x, y, t) &= \sum_{m=0}^M \sum_{n=0}^N \psi_{mn}(t) \psi_m(x) \psi_n(y) \\ T(x, y, t) &= \sum_{m=0}^M \sum_{n=0}^N T_{mn}(t) \phi_m(x) \phi_n(y) + x - y \end{aligned} \right\} \quad (20)$$

Where M and N indicates the truncation number in the x and y axis respectively, and the coefficient of expansion is represented as w_{mn} , ψ_{mn} and T_{mn} . To acquire time dependent evaluation of $\bar{w}(x, y)$, $\bar{\psi}(x, y)$ and $\bar{T}(x, y)$, the requisite series expansion (19) is then transferred into the basic equations (14), (15) and (16) abide by applying the collocation method. As a consequence, a set of nonlinear algebraic equations for w_{mn} , ψ_{mn} and T_{mn} are attained. To recognize more detailed about the spectral method and function expansion together with collocation method has been intimated by Mondal et al. [16], and Gottlieb and Orszag [50].

3.2 Time-evolution Calculation

Unsteady solutions of the fluid flow through the curved duct are calculated by using the Crank-Nicolson and Adams-Basforth methods together with the expansion of the function (20) and the collocation method. Here, equation (21) to (23) can be found after using the Crank-Nicolson and the Adams-Basforth method in the non-dimensional zed equation (14) to (16) as:

$$\left(\frac{1}{\Delta t} - \frac{\Delta_2}{2} \right) w(t + \Delta t) = \left(\frac{1}{\Delta t} + \frac{\Delta_2}{2} \right) w(t) - \delta x \frac{w(t) - w(t - \Delta t)}{\Delta t} + D_n + \delta x \Delta_2 w(t) - \frac{\delta^2 w(t)}{1 + \delta x} + \delta \frac{\partial w(t)}{\partial x} + \frac{3}{2} \bar{P}(t) - \frac{1}{2} \bar{P}(t - \Delta t), \quad (21)$$

$$\left(\frac{1}{\Delta t} - \frac{\Delta_2}{2} \right) \Delta_2 \psi(t + \Delta t) = \left(\frac{1}{\Delta t} + \frac{\Delta_2}{2} \right) \Delta_2 \psi(t) + \frac{\delta}{1 + \delta x} \frac{1}{\Delta t} \left(\frac{\partial \psi(t)}{\partial x} - \frac{\partial \psi(t - \Delta t)}{\partial x} \right) + \frac{\delta}{(1 + \delta x)^2} \left\{ -2(1 + \delta x) \frac{\partial}{\partial x} \Delta_2 \psi(t) + 3\delta \frac{\partial^2 \psi(t)}{\partial x^2} - \frac{3\delta^2}{(1 + \delta x)} \frac{\partial \psi(t)}{\partial x} \right\} - Gr(1 + \delta x) \frac{\partial T(t)}{\partial x} + \frac{3}{2} \bar{Q}(t) - \frac{1}{2} \bar{Q}(t - \Delta t) \quad (22)$$

$$\left(\frac{1}{\Delta t} - \frac{\Delta_2}{2Pr} \right) T(t + \Delta t) = \left(\frac{1}{\Delta t} + \frac{\Delta_2}{2Pr} \right) T(t) - \delta x \frac{T(t) - T(t - \Delta t)}{\Delta t} + \frac{1}{Pr} \delta \left(x \Delta_2 T(t) + \frac{\partial T(t)}{\partial x} \right) + \frac{3}{2} \bar{R}(t) - \frac{1}{2} \bar{R}(t - \Delta t). \quad (23)$$

Numerical calculations are performed only for $w(t + \Delta t)$, $\psi(t + \Delta t)$ and $T(t + \Delta t)$.

3.3 Resistance Coefficient

Resistance coefficient which is also acquainted as the hydraulic resistance coefficient played a significant role in fluid dynamics. It predominantly illustrated us how much the axial flow is interrupted at the duct wall and mathematically it can be written as

$$\frac{P_1^* - P_2^*}{\Delta z^*} = \frac{\lambda}{d_h^*} \frac{1}{2} \rho \langle \omega^* \rangle^2 \quad (24)$$

Here, $(P_1^* - P_2^*) / \Delta z^* = G$, is said as pressure gradient parameter and the resistance coefficient, λ is defined as the average of the dimensionless axial velocity $\langle w \rangle$, is also presented by

$$\lambda = \frac{4\sqrt{2\delta} Dn}{\langle w \rangle^2} \quad (25)$$

In the above, P_1^* and P_2^* denote the quantities of dimensional ones, $\langle \omega^* \rangle$ acts as the average over the cross section of the duct and d_h^* is the hydraulic diameter. The original axial velocity $\langle w \rangle$ is computed by

$$\langle w^* \rangle = \frac{v}{4\sqrt{2\delta} l} \int_{-1}^1 dx \int_{-1}^1 \omega(x, y, t) dy \quad (26)$$

Herein, equation (26) will be needed to determine the resistance coefficient of the flow evolution by numerical computation.

3.4 The Nusselt Number

In curved duct, theoretically Nusselt number is illustrated as the proportion between the convective and the conductive heat transfer across the frontier. As the time independent solution and the dependent behavior are calculated in several ways in the ducting system so the mathematical representation of the Nusselt number revealed differently. The indicia of heat transmission, the Nusselt number, Nu , for steady solution can be expressed as

$$Nu = - \frac{d^*}{\Delta T^*} \left\langle \frac{\partial T^*}{\partial x^*} \right\rangle_{x=0}. \quad (27)$$

Here the dimensionless quantities and the average over the heat transportation from the fluid from the duct walls are denoted by asterisk (*) and $\langle \rangle$, the distance of the walls are implies as x , the distinction of temperature between the cooled and heated side walls are defined as ΔT .

Again the Nusselt number, for the unsteady solution at the cooled side walls and the heated side walls can be written as follows:

$$Nu_{\tau_c} = \frac{1}{2} \int_{-1}^1 \left\langle \left\langle \frac{\partial T}{\partial x} \right|_{x=-1} \right\rangle \right\rangle dy, \quad Nu_{\tau_h} = \frac{1}{2} \int_{-1}^1 \left\langle \left\langle \frac{\partial T}{\partial x} \right|_{x=1} \right\rangle \right\rangle dy \quad (28)$$

Here the average of the time interval, is denoted by \cdot . For the periodic oscillation, usually \cdot is chosen as one period and if the oscillation is chaotic, \cdot is taken as an suitable time interval.

3.5 Grid Efficiency

Grid efficiency confirms the validity of the algorithm of governing equations. Wang et al. [51] have calculated the change of bifurcation structure for changing the grid

points. Mondal et al. [16] have also enumerated the numerical accuracy of their algorithm for curved square duct by fixing the parameters. But these studies have not discussed the percentage error. Here, the numerical accuracy has been checked out for both positive and negative rotation. The numerical accuracy has been measured by taking the resistance coefficient and the axial flow of the duct. We have also computed the percentage error for both the resistance coefficient and axial flows by changing the grid size. The percentage errors are defined

as, $\varepsilon_p = \text{abs} \left(\frac{\text{current value} - \text{previous value}}{\text{current value}} \right) \times 100\%$. The grid efficiency is represented in Table 1 for $Tr = 1000$ and $Tr = -1000$, and the errors are also represented by the pie chart as shown in Figure 2. The pie chart of the left and right side bears the accuracy of resistance coefficient and axial flow for changing the grid size respectively. It has been demonstrated that the grid accuracy is accurate enough without any doubt and for increasing the grid size the percentage errors are decreased. In this investigation, M and N are designated as the grid size and we have used $M=22$ and $N=22$.

Table 1. Values of resistance coefficient and axial flow for different grid points

Taylor Numbers	M	N	λ	Percent Relative error (ε_p) of λ	$w(0,0)$	Percent Relative error (ε_p) of w
Tr = 1000	14	14	0.1304543908819534		380.5599184058002	
	16	16	0.1302482460742482	0.158271	379.6114065490499	0.249864
	18	18	0.1285711795042113	1.304388	381.0939973340698	0.389035
	20	20	0.1293940463294373	0.635939	378.4383971745747	0.701726
	22	22	0.1294101241050988	0.012434	378.2344608734196	0.053918
	24	24	0.1293810483049980	0.022473	378.4453986048577	0.055738
Tr = - 1000	14	14	0.1181315100105367		385.9437054352970	
	16	16	0.1177767609013260	0.301205	385.2908272855017	0.169451
	18	18	0.1174844780220167	0.248784	381.7489233710441	0.927812
	20	20	0.1174137857313868	0.060208	383.2689206419709	0.396588
	22	22	0.1174495381464427	0.030441	383.3833886118026	0.029857
	24	24	0.1174420404854840	0.006384	383.4798157380512	0.025145

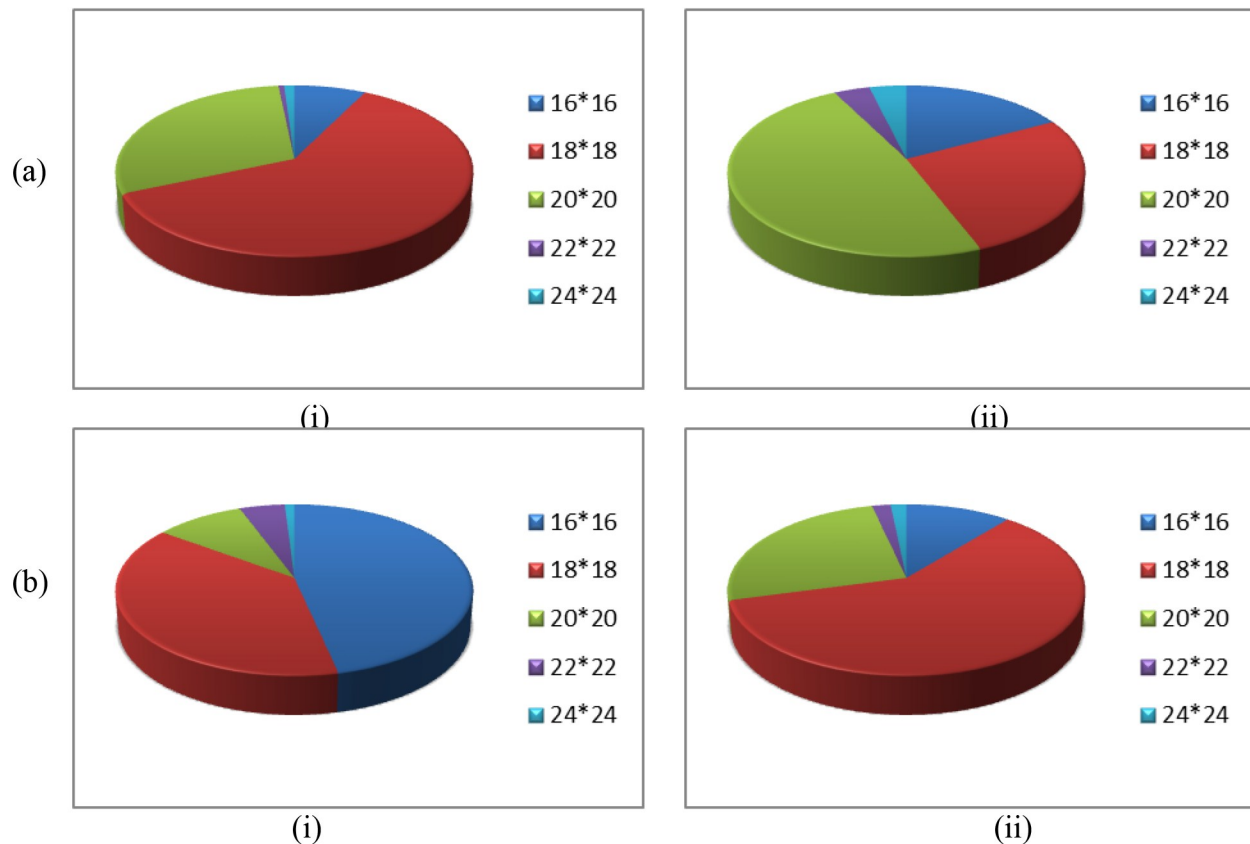
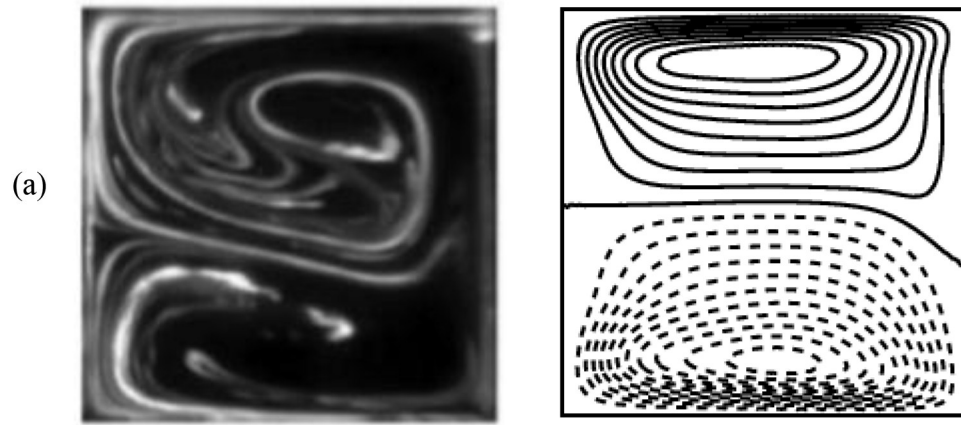


Figure 2. Pie chart of the numerical accuracy table (a) positive rotation, (b) negative rotation; (i) resistance coefficient, (ii) axial flow.

3.6 Numerical validation with the experimental results

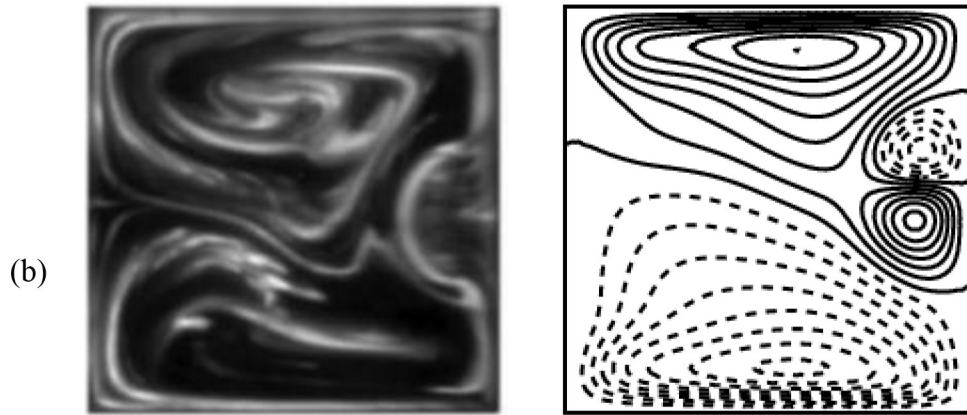
From the grid accuracy, it is seen that the formulation and the coding of the governing equations of the curved duct are accurate enough. Now, we have investigated the authentication of the numerical data with the experimental result. Yamamoto et al. [52] are only the first investigators, who have revealed the experimental outcome for both positive and negative rotation. Not only did they perform for a different Dean number with a fixed Taylor number both positively and negatively but also have manifested for different Dean and Taylor numbers. Water is the main flow in their experiment where they have taken this in an overflow tank. They have also synthesized a specific amount of pigment that has mixed with alcohol so that the mixture has equalized to the weight of water. A motor has been included at the inner disk for which it can be rotated around the center of the duct. After forming the experimental setup, they have injected fluid in the duct with keeping the rotational speed fixed for both positive and negative

rotation. For changing the Dean number, they have captured some photos. After observing these, they have also taken some photos by changing the Dean and Taylor number. It is observed that the experiment is conducted for the curvature 0.03 and aspect ratio 1. To validate with the numerical data with experimental results, we have transformed the magnitude of the parameters as same as their study. Then we have fixed the rotation and increased the pressure gradient in the curved duct. After getting some numerical data, we have sketched out the graph. It has demonstrated that the numerical data are almost the same as the experimental results. We have again executed the numerical investigation for different Dean and Taylor number which is also nearly same as the experimental results. So the methodology of the present paper is sufficiently excellent. Figure 3 represents the validation of the numerical and experimental result. The numerical outcomes (right side) have been investigated by the authors and the experimental view (left side) of secondary flow has been found by Yamamoto et al. [52].



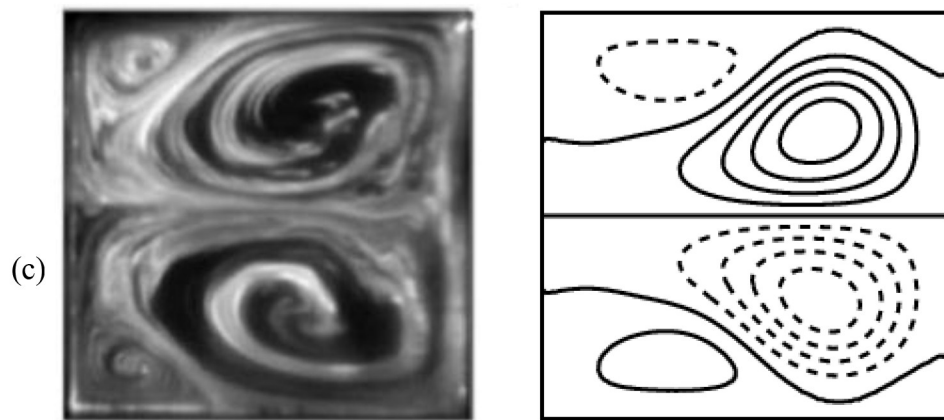
Dn=146

Dn=150



Dn=176

Dn=185



Dn=32.36

Dn=40

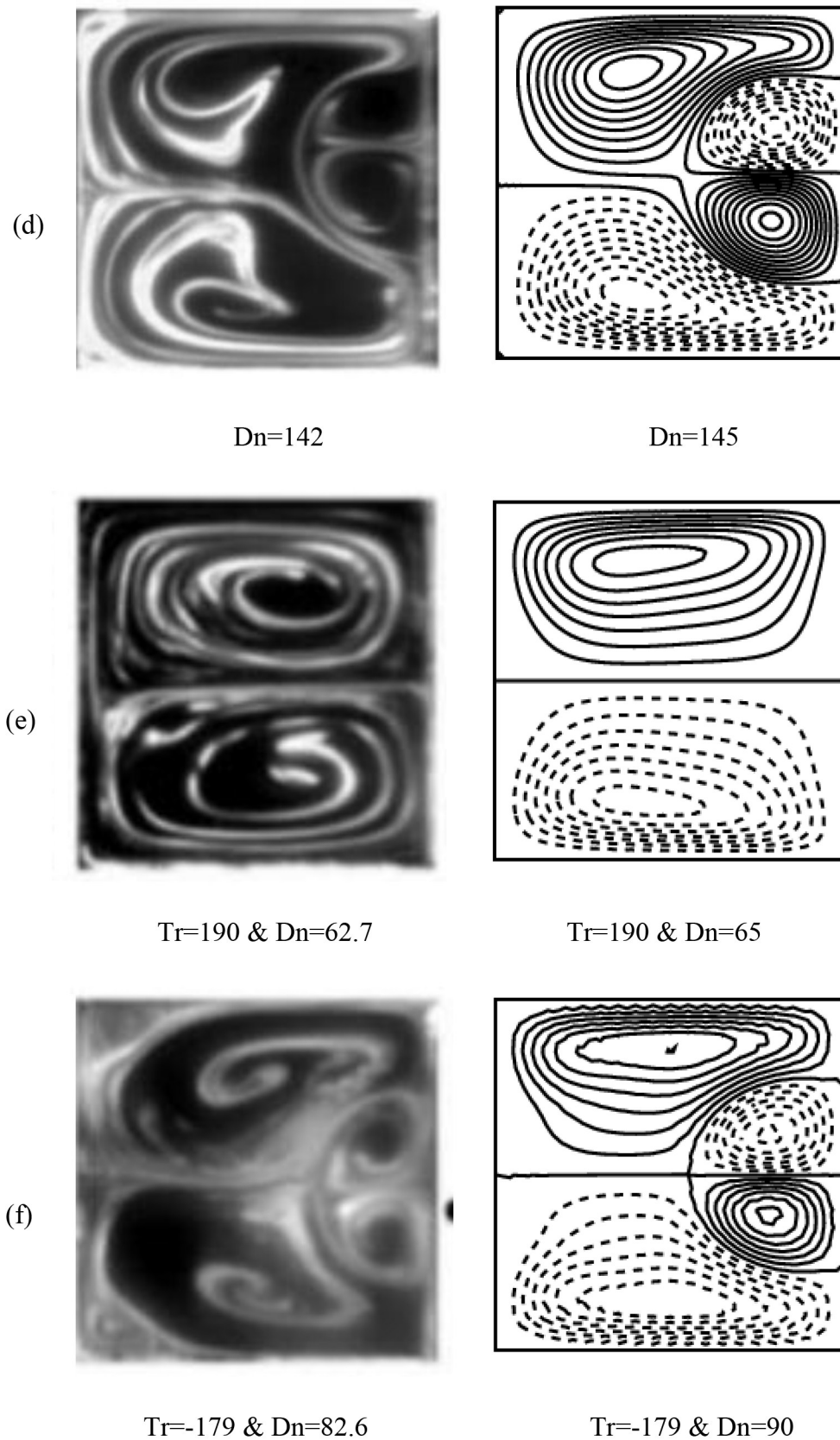


Figure 3. Comparison between the numerical result (right side) with the experimental data (left side) for, (a, b) positive rotation, (c, d) negative rotation, (e, f) changing with the Dean and Taylor number both positive and negative direction.

4. RESULTS AND DISCUSSIONS

In the following, steady solution branches with linear stability have been illustrated for the positive rotation where the analyzing data have been attained by implementing a spectral method with the Newton-Raphson method. Here, the work has been mainly conducted for a fixed Dean number ($De = 1000$), Grashof number ($Gr = 100$) and curvature ($\delta = 0.01$) where the rotational parameter, the Taylor number has been varied from 0 to 2500. After finding out the steady solution branches, time-evolution calculation of the unsteady solution has been performed in the range for a fixed difference (250). Moreover, the temperature gradients for different Taylor numbers have been also calculated. Two types of flow velocity axial and the secondary flow and the temperature profiles have been also explored which proves that there is a good connection between the steady solution, linear stability, unsteady solution, and temperature gradients. The same work has been also conducted here for the negative rotation from $Tr = -10$ to $Tr = -2500$ after completing the positive rotation.

4.1 Positive Rotation

4.1.1 The steady solution branches

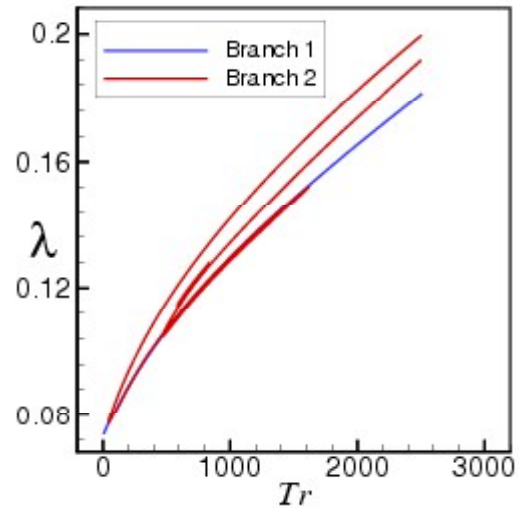


Figure 4. Steady solution branches for $0 \leq Tr \leq 2500$.

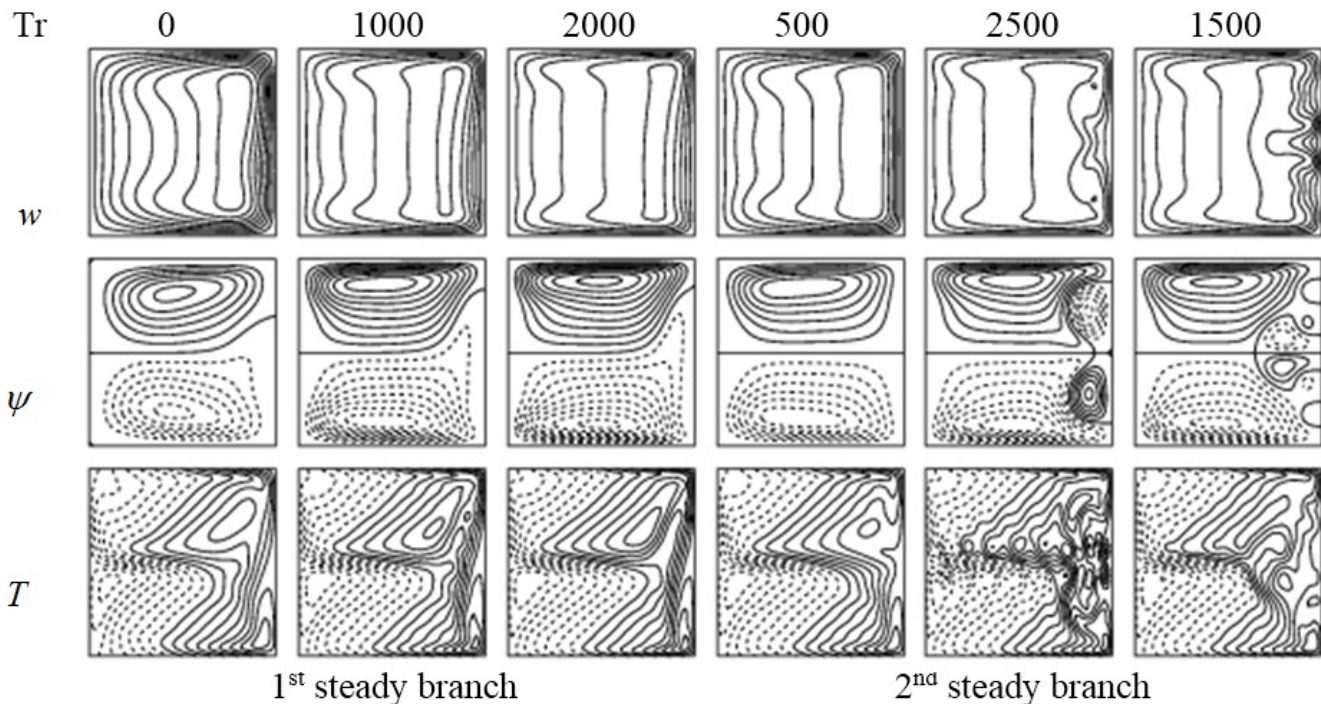


Figure 5. Contours of axial velocity (topmost), stream function (central), isotherms (lowermost) for several Taylor numbers.

With the help of path continuation technique, two steady solution branches have been found for several initial suppositions. The two steady branches are addressed as the 1st steady branch and the 2nd steady branch where the 1st and 2nd steady branch is depicted by the blue and red solid line as shown in Figure 4 respectively. It has seen that the 1st steady solution branch has no turnings within the range of Taylor number and the 2nd steady solution branch

has arrived at the destination with various turnings. A detailed explanation of the respective two steady branches has been imparted below. Two types of flow velocity, axial and secondary flow, and temperature profiles are shown in Figure 5. From the axial flow, it is said that the axial flows are pushed the inner wall of the duct and two to eight vortex symmetric and asymmetric secondary flows have formed for the required ranges of Taylor number.

4.1.1.1 The first steady solution branch

The 1st steady solution branch is explored in Figure 6 and it is said that this is the only branch which covers throughout the entire range of Taylor number. It starts from the point a of $Tr = 0$ and without any turnings, it ends at point b of $Tr = 2500$. Axial flow, secondary flow, and temperature profiles have been represented in Figure 7. It has been demonstrated from the secondary flow patterns that the upper wall of the duct has been shrunk by the asymmetric line.

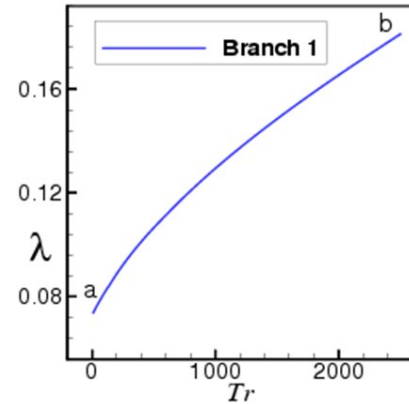


Figure 6. 1st steady solution branch for $Dn=1000$, $Gr=100$, $\delta=0.01$ and $0 \leq Tr \leq 2500$.

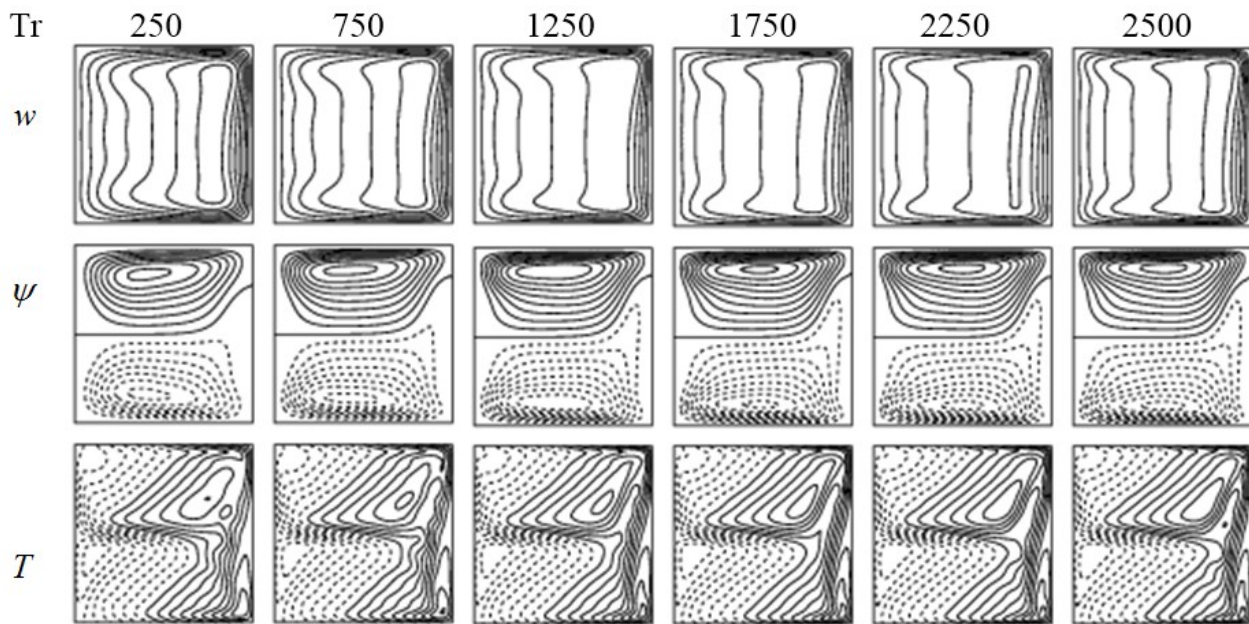


Figure 7. Contours of axial velocity (topmost), stream function (central), isotherms (lowermost) for several Taylor numbers.

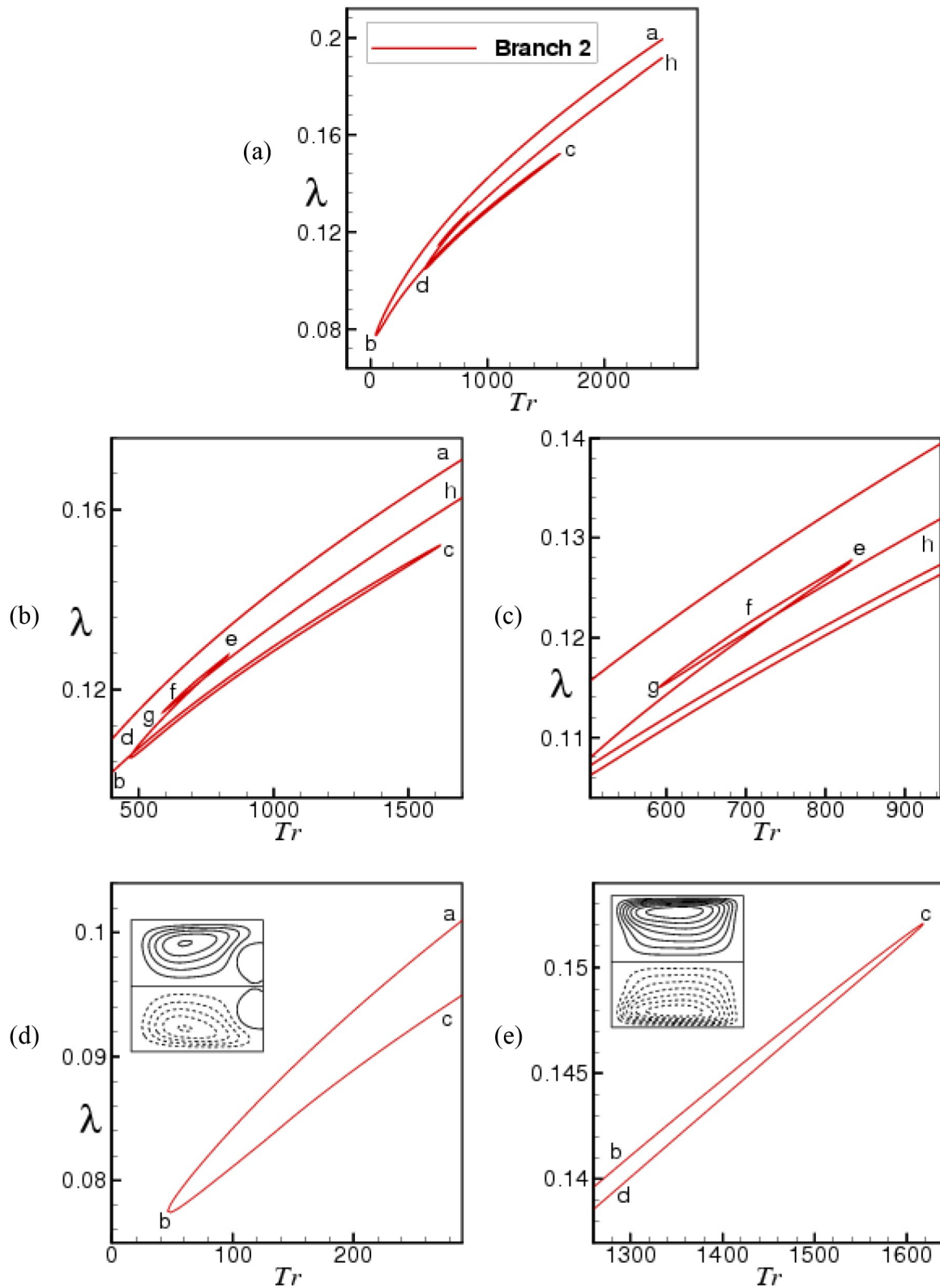
4.1.1.2 The second steady solution branch

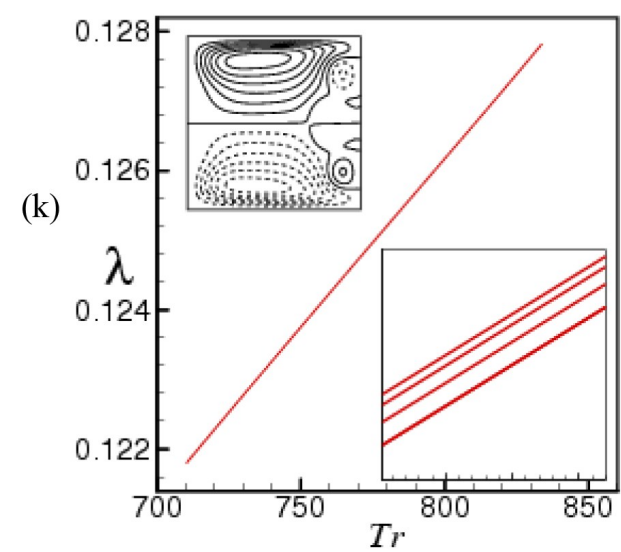
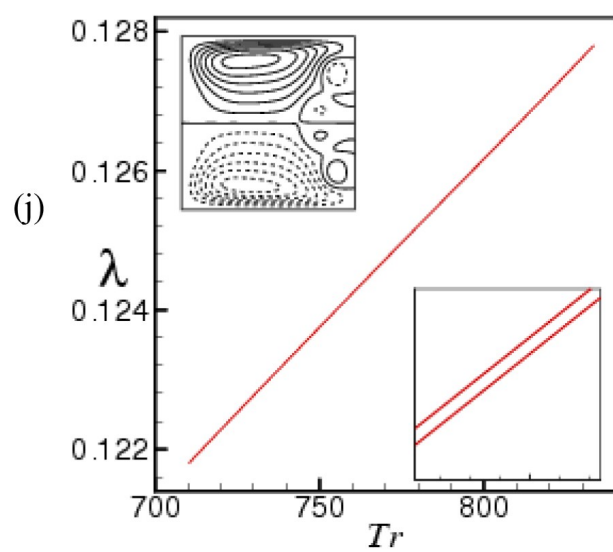
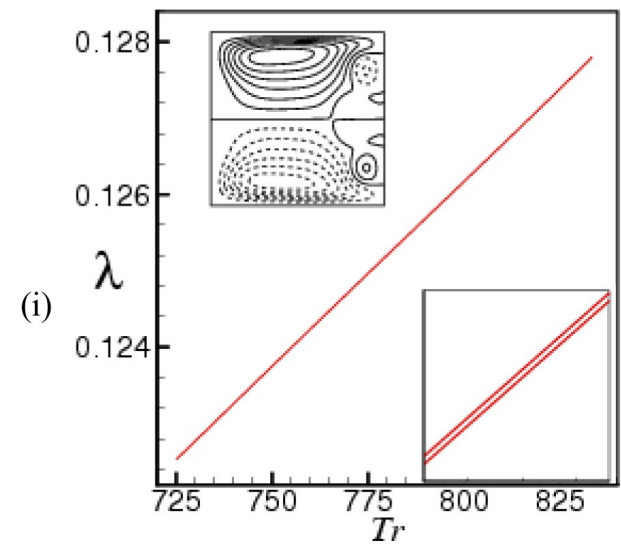
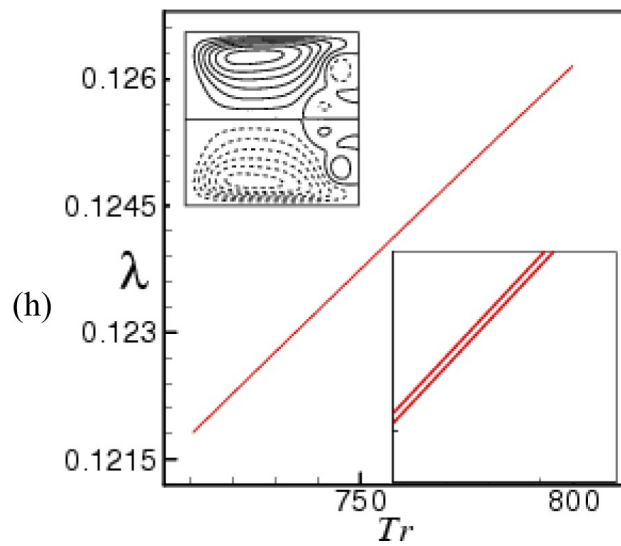
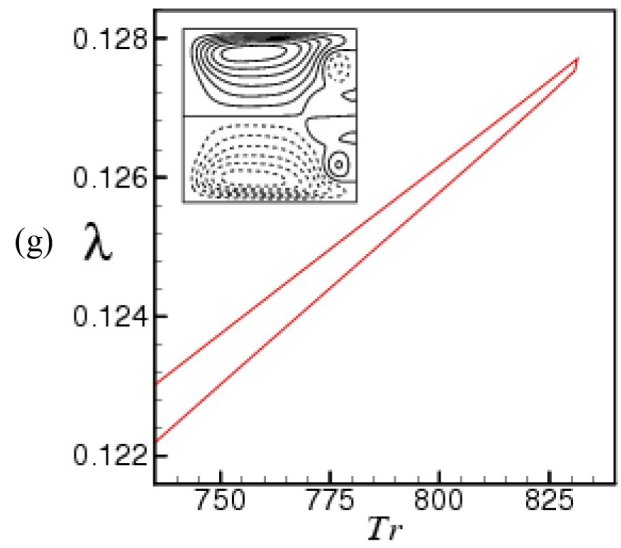
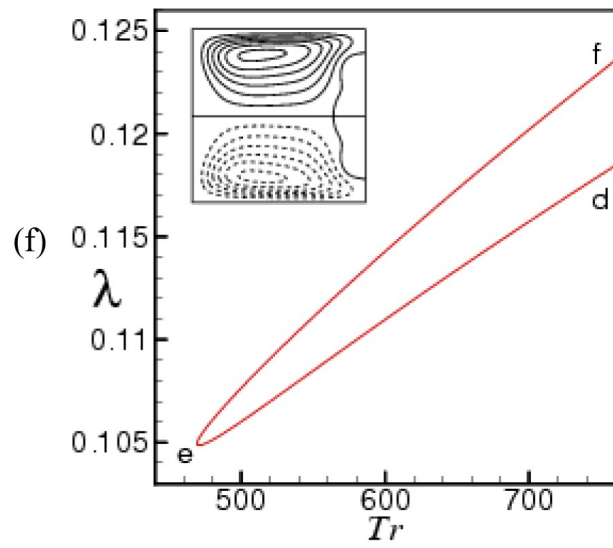
The 2nd steady branch is designated in Figure 8 (a) and it has been seen that various types of turnings have happened between the required ranges of Taylor number. Figure 8 (b) & (c) have displayed the enlargement of the turnings of Figure 8 (a). It has started from the point a of $Tr = 2500$ and gone backward for decreasing the resistance coefficient. At $Tr = 46.145$ (Figure 8 (d)), it turns, and the resistance coefficient has climbed up for increasing the Taylor number. The steady branch has again inclined at c of $Tr = 1617.47$ (Figure 8 (e)) and at the point d of $Tr = 469.80$ (Figure 8 (f)), it has further turned. It has been noted that more turning and overlapping have occurred from point d to g. After the point of g at $Tr = 591.63$ (Figure 2 (t)), the path has ended at h.

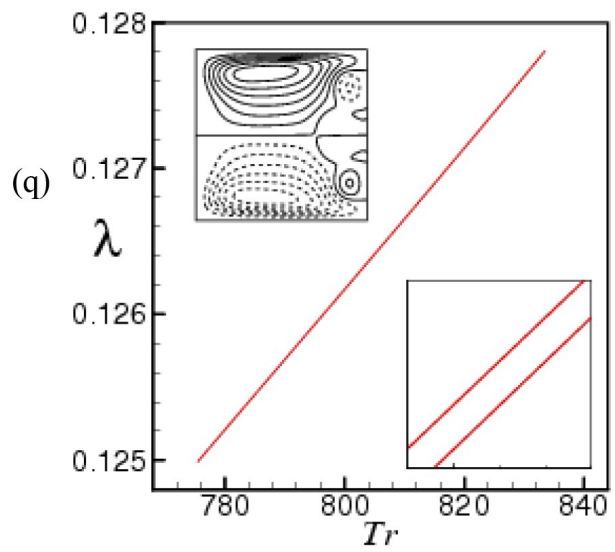
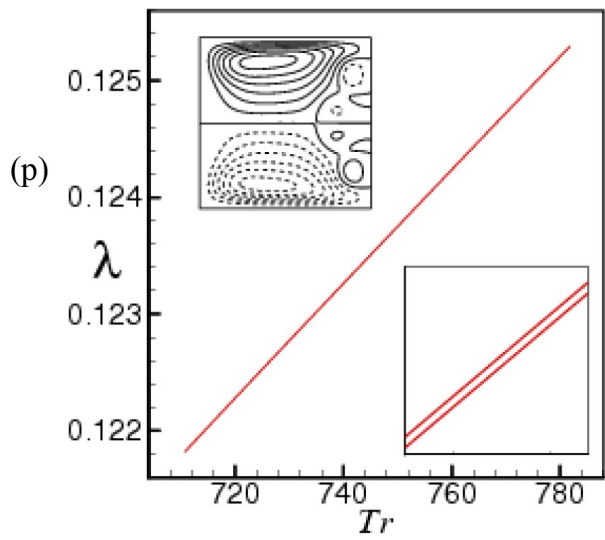
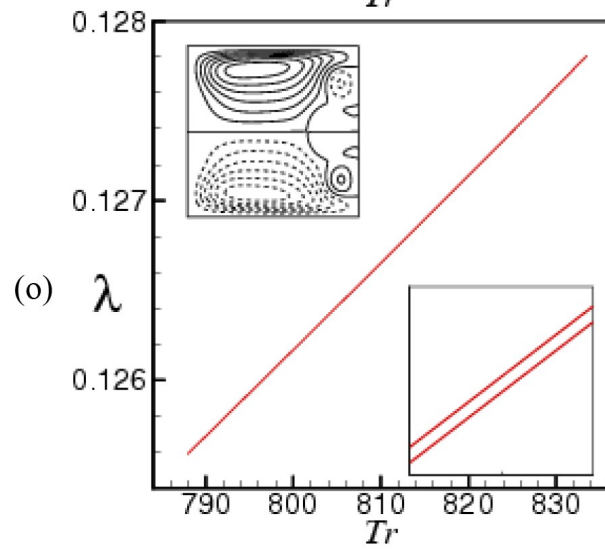
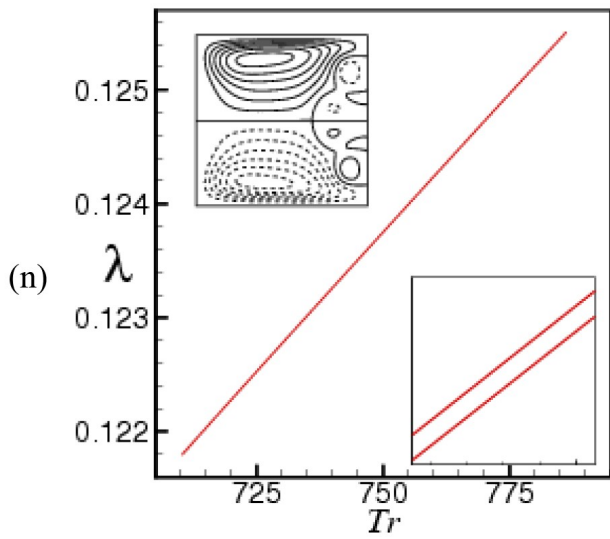
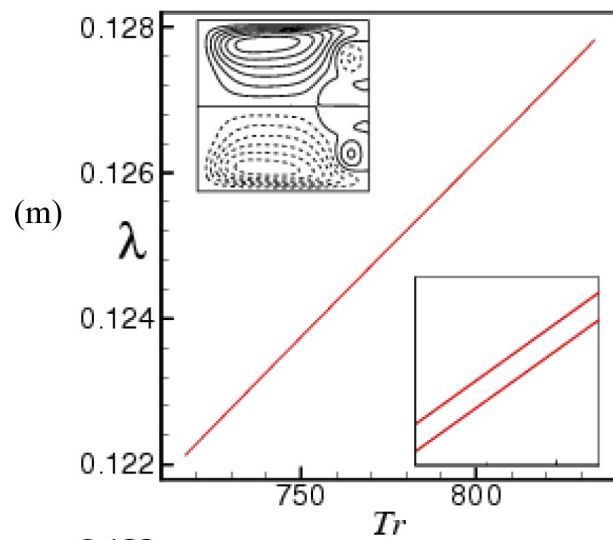
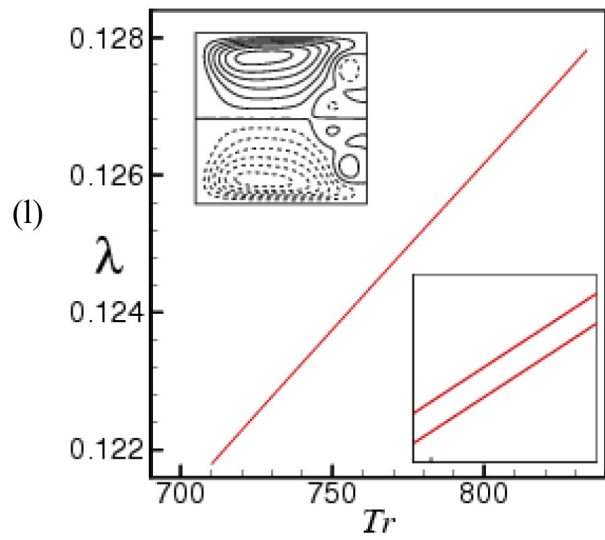
The enlargement of turning points of the branch from f to g is also included in Figure 8 (g) to 8 (s). Looking at the images of Figure 8 (g) to 8 (s), it looks like there is only one line that appears, but when we enlarge the images, it is seen that the lines have fallen on each other. Contours of axial flow, secondary flow and temperature profiles of the curved duct are shown in Figure 9. Axial flows show that the velocity parallel to the horizontal walls has created the high-velocity region for enhancing the rotational parameters. Streamlines of secondary flow patterns show that the two vortex secondary flows are altered into symmetric four vortices at the point b of and the number of vortices has been decreased at the turned point c of . At point d, the symmetric secondary vortices have been compressed at the upper and lower wall and a new region is formed at the outer wall of the duct. Due to increasing the Coriolis force more, the two vortex solution is converted into six vortex asymmetric secondary flow as

shown in Figure 8 (g) for $\lambda = 0.11$. The asymmetric six vortex solution is also changed into symmetric eight vortex at (Figure 8(h)). These symmetric and asymmetric six and eight vortex solutions are shown till the end of turnings where the six

vortex of asymmetric solutions are in Figure 8 (g, i, k, m, q) at $\lambda = 0.11$ and symmetric in Figure 8 (f, o) for $\lambda = 0.11$ and eight vortex of asymmetric are in Figure 8 (j, l, p, r) for $\lambda = 0.11$ and symmetric for in Figure 8 (h, n, t).







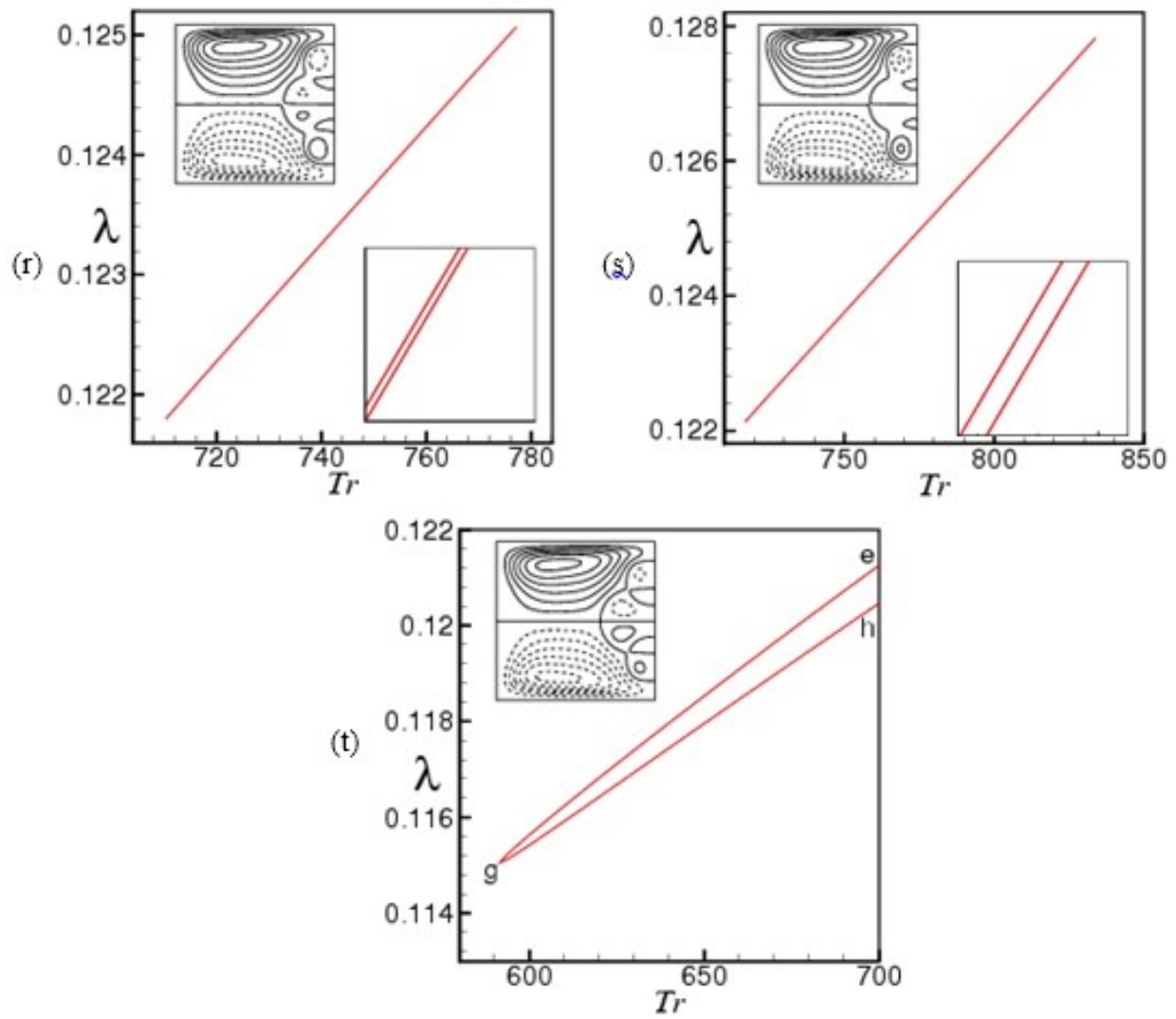


Figure 8. 2nd steady solution branch and the turnings for $Dn = 1000$, $Gr=100$, $\delta=0.01$ and $0 \leq Tr \leq 2500$.

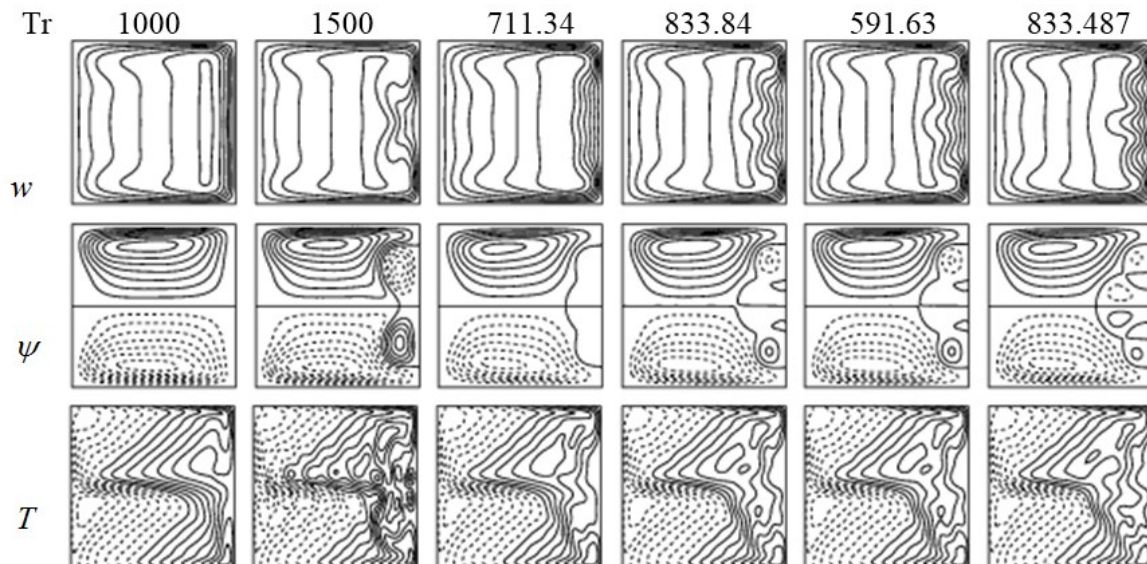


Figure 9. Contours of axial velocity (topmost), stream function (central), isotherms (lowermost) for several Taylor numbers.

4.1.2 Linear Stability analysis:

Linear stability analysis creates a connection between the time-independent and time-dependent oscillations. So, linear stable and unstable points have been calculated here from the steady solution branches. Firstly, it is performed alongside x and y -axis where z is taken as an independent. It is resolved by the collocation method using the function expansion formula which is also built the linear equalization of the perturbation $w(x, y)$ and $\psi(x, y)$. Here, $e^{\sigma t}$ is designated as the time-dependent perturbations, where σ sigma is considered as, $\sigma = \sigma_r + i\sigma_i$. The steady-state solution shows the linear stability if the real portion of the σ_r of the eigenvalue is not positive but if there has at

most one positive real part, it shows that it is linearly unstable. In the unstable territory, the perturbation climbs monotonically for $\sigma_i = 0$ and oscillatory for $\sigma_i \neq 0$. After investigating the linear stability, the outcomes are presented in Table 2 for positive rotation. It has seen that the 1st steady branch represents the linear unstable throughout the whole region whereas 2nd steady branch also shows a linear unstable region by showing a small stable region. The linear stable points are presented with the italic and the sequential part of stable and unstable points are indicated by the bold. The graphical representation of the 1st and 2nd steady branches are also displayed in Figure 10 (a) & (b) where a small portion of the stable region is designated by the black bold solid line.

Table 2. Stability analysis for the curved duct between $0 \leq Tr \leq 2500$

Tr	λ	σ_r	σ_i	Criteria
100	0.0814504579628859	3.1953×10^1	0	Linear Unstable
167.95	0.0865316895237187	1.2650×10^{-3}	-1.9410×10^1	Linear Unstable
167.96	0.0865324540063056	-6.8598×10^{-4}	1.9413×10^1	<i>Linear Stable</i>
250	0.0925183273975206	-1.9159	0	<i>Linear stable</i>
500	0.1069195427764804	-2.0879	0	<i>Linear stable</i>
688.25	0.1161695915285333	-4.5196×10^{-5}	7.6423×10^1	<i>Linear stable</i>
688.26	0.1161700532219283	2.9631×10^{-4}	7.6424×10^1	Linear Unstable
750	0.1190189477387698	2.1381	8.0194×10^1	Linear Unstable
1000	0.1295683848832986	9.9843	-9.3269×10^1	Linear Unstable
1250	0.1533208081515658	1.5287×10^2	0	Linear Unstable
1500	0.1636070126985024	1.6238×10^2	0	Linear Unstable
2000	0.1822503141667548	1.7334×10^2	0	Linear Unstable
2500	0.1995118925289715	1.6828×10^2	0	Linear Unstable

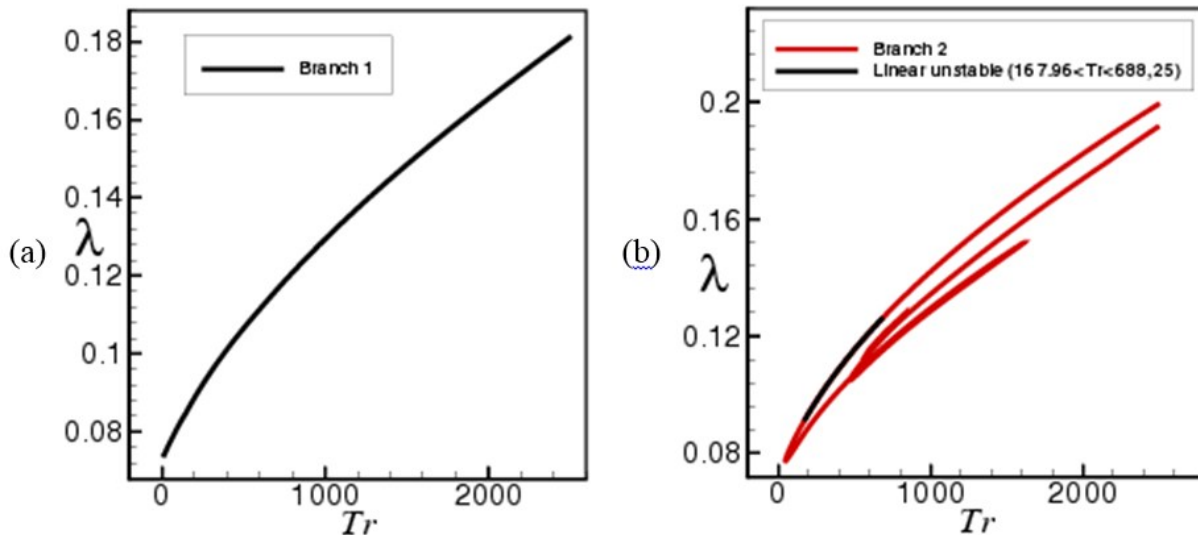


Figure 10. Linear stable regions, (a) 1st steady branch, (b) 2nd steady branch.

4.1.3 Vortex structures in steady solution for positive rotation

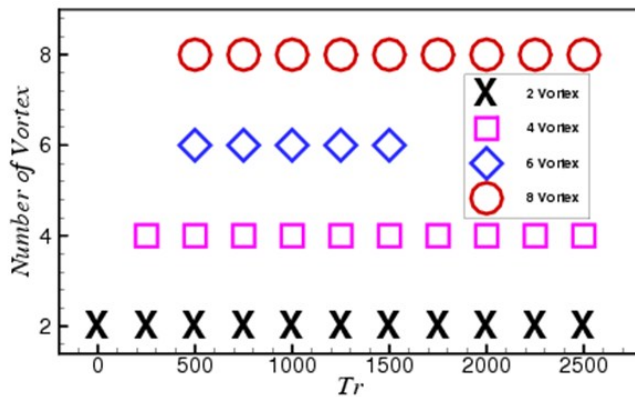


Figure 11. Vortex structures of the steady solution branches for several Taylor numbers ($0 \leq Tr \leq 2500$).

Vortex structures not only describe the number of vortex structures of the duct but also give about the statement of fluid mixing and heat transfer through the duct. Secondary vortices for several Taylor numbers have been sketched in Figure 11 at the " Tr vs. Number of vortex" plane. In the current investigation, two-, four-, six-, eight-vortex flow structures have been found for 1st and 2nd steady solution branches. Here, only two vortex have consisted only for the 1st steady branch whereas two to eight vortex have created for 2nd steady branch. The number of vortices in the second branch has risen because of the turnings of the branch, where the turnings have been generated for the centrifugal force of the duct. Here, the two-, four-, six-, eight- vortex have been represented as cross, square, diamond and circle respectively. It is seen that two and four vortex have been found throughout the entire range of Taylor number $0 \leq Tr \leq 2500$. The six vortex have been formed between $500 \leq Tr \leq 1500$ and the eight vortex solutions has been established within $500 \leq Tr \leq 2500$. It has also demonstrated that the number of vortex is influenced by the rotation, turnings, and curvature of the duct. In the vortex structure of the steady solution, we don't get any odd number of vortex in the secondary flow but it is contained in the steady branches and investigated by the time evolution calculation, which has been discussed in section 4.1.5.

4.1.4 Time evolution calculations

Time evolution calculations of the unsteady solution have been performed here for an extensive range of Taylor number ($0 \leq Tr \leq 2500$) where the others parameters are fixed. The programming algorithm of the governing equations has been developed with the Crank-Nicolson method, Adam-Bashforth method and function collocation method simultaneously.

When $Tr = 0$, time evolution calculation of the unsteady solution is plotted in Figure 12 (a) in the *time vs. resistance coefficient* plane. It has seen that the unsteady observation gives the multi-periodic result, which has been also endorsed by the phase space and power spectrum analysis in Figure 12 (b) & (c). Here, the phase space which has been calculated from the unsteady solutions sketched in $\lambda-\gamma$ plane, and the symbol γ is prescribed as $\gamma = \iint \psi dx dy$. The power spectrum in Figure 12 (b) has narrated as the ability of the tremble as a function of frequency at which the frequencies have potent and at which the frequencies are feeble. It is said from the Figure 12 (c) that multiple orbits have been constructed in phase space plane and the line spectrum of the fundamental frequency and its harmonics have been infirmed gradually at the *frequency vs. power spectrum* plane. Two types of flow velocity axial and secondary flow and temperature profiles are shown in Figure 13. It has been already known from the axial flow of the positive rotation of the duct that it has pushed at the inner wall of the duct. From the secondary flow, two up to four vortex solution has been found for $Tr = 0$. It has already seen that there is a strong bond between the axial and the secondary flow. At $t = 20.40$ & 20.70 , two high-velocity regions have made at the outer wall of the duct, as a result, two new vortices have generated which are known as Ekman vortices. It has also seen that the two new vortices at $t = 20.40$ are smaller than that $t = 20.70$. At $t = 20.40$, only two high-velocity regions are created whereas two high-velocity regions with two dumbbells have consisted at the outer wall of the duct. So, the secondary flow at $t = 20.70$ is stronger enough than $t = 20.40$. This has created because of the centrifugal force of the duct. Temperature profiles show that the heat has transferred exceedingly at $t = 20.40$ & 20.70 with in the time ($20.30 \leq t \leq 20.80$). It is easily demonstrated that when the flow velocity is strong, the heat is more transferred which proves that the fluid is mixed more when the velocity of the flows are strong.

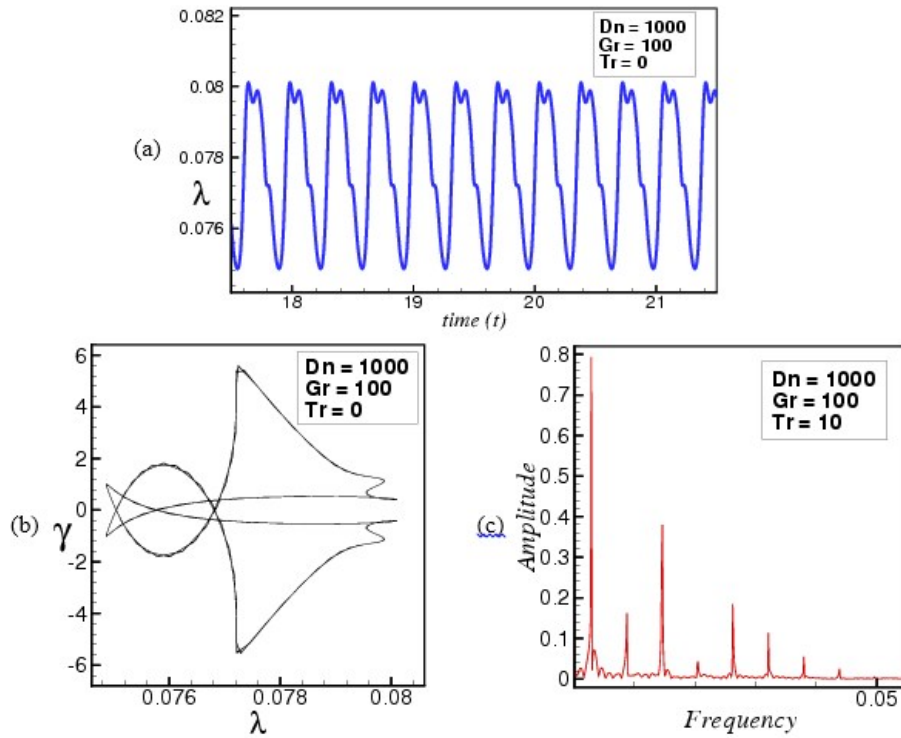


Figure 12. (a) Time dependent behavior in $t - \lambda$ plane, (b) Phase space, (c) Power spectrum, for $Tr = 0$.

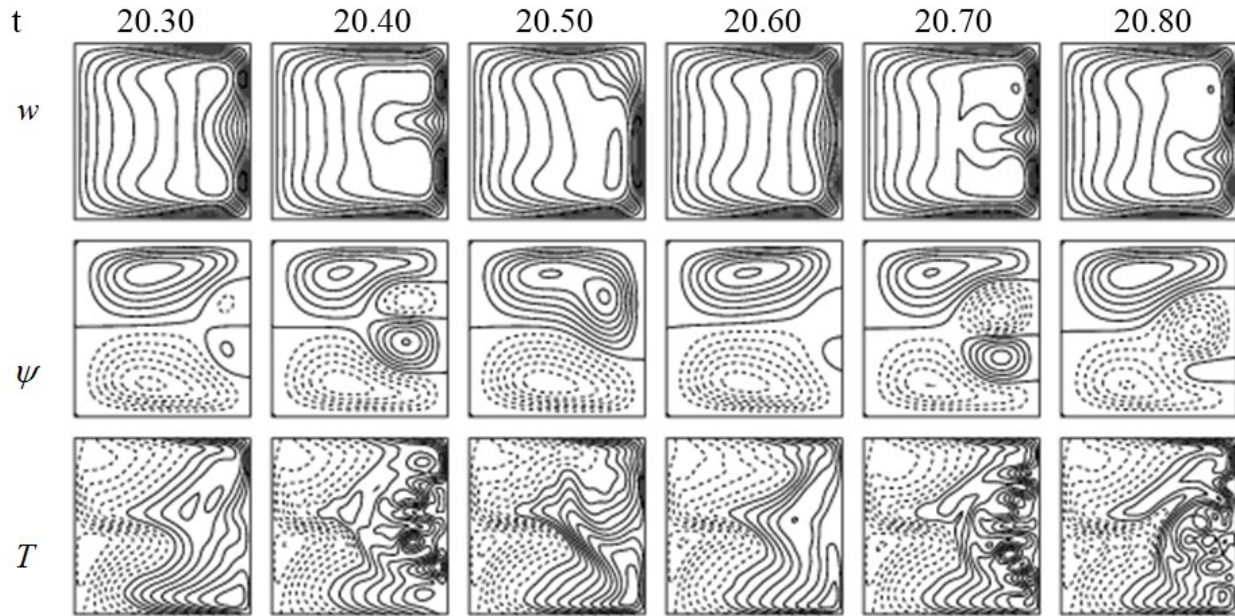


Figure 13. Contours of axial velocity (topmost), stream function (central), isotherm (lowermost) for various Dean numbers at $Tr = 0$.

If the rotational speed of the duct is increased, then the multi-periodic oscillation covers into a steady-state solution from $Tr = 167.96$, which is also justified by the linear stability analysis. The steady-state solution is continued up to $Tr = 688.26$. Figure 14 (a) shows the

steady-state solutions for $Tr = 250$ & 500 . Axial flow, secondary flow, and temperature profiles are visualized in Figure 14 (b). It is said from the steady-state solutions that symmetric two vortex patterns have been found only.

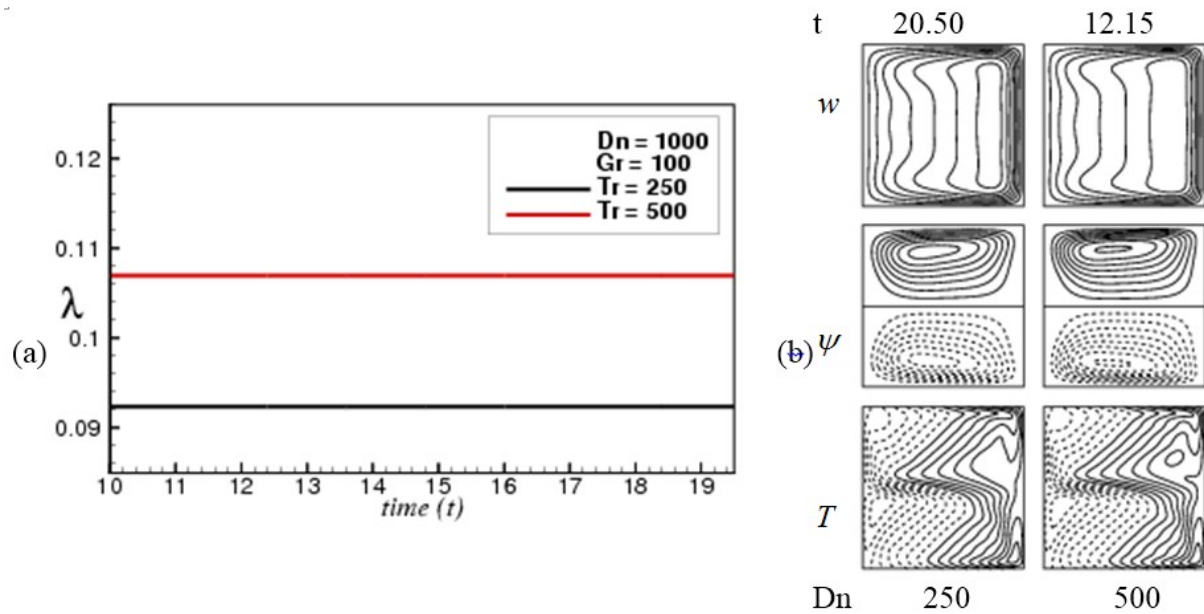


Figure 14. (a) Time dependent behavior in $t - \lambda$ plane, (b) Contours of axial velocity (topmost), stream function (central), isotherm (lowermost) for various Dean numbers at $Tr = 250$ & 500 .

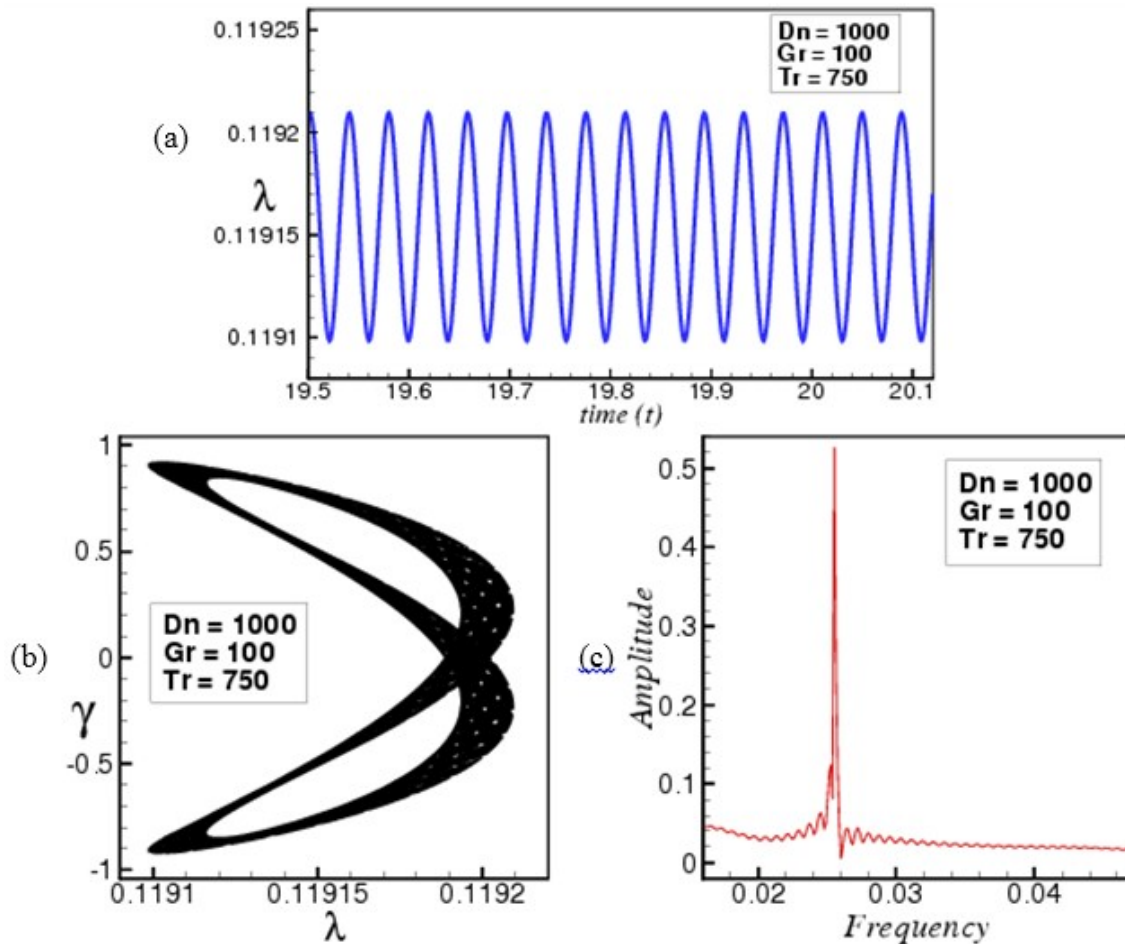


Figure 15. (a) Time dependent behavior in $t - \lambda$ plane, (b) Phase space, (c) Power spectrum, for $Tr = 750$.

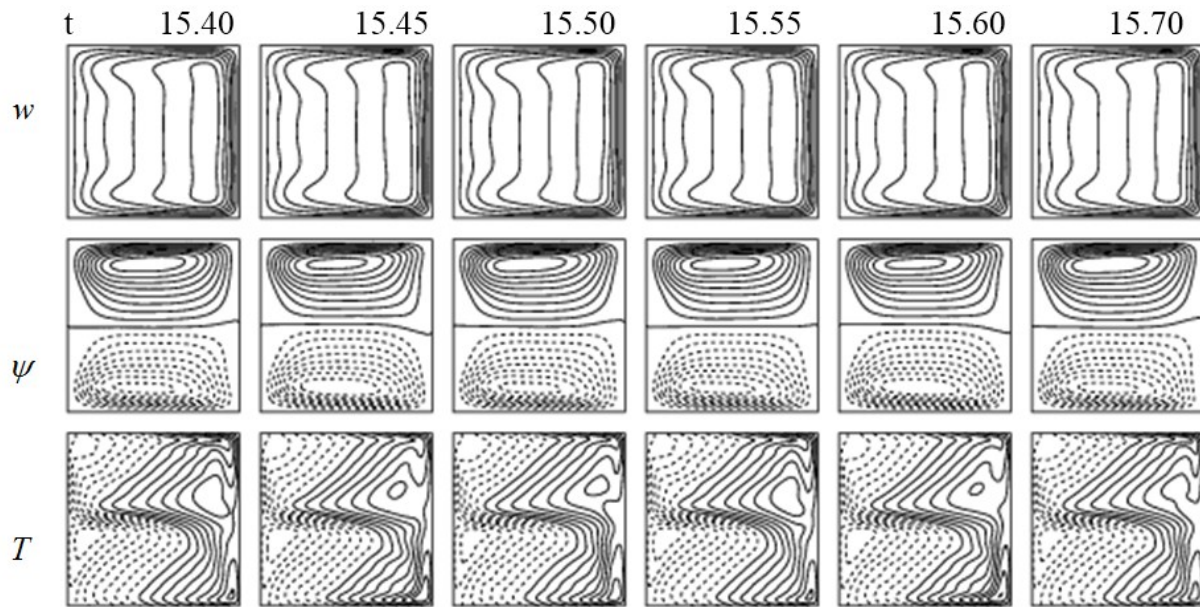


Figure 16. Contours of axial velocity (topmost), stream function (central), isotherm (lowermost) for various Dean numbers at $Tr = 750$.

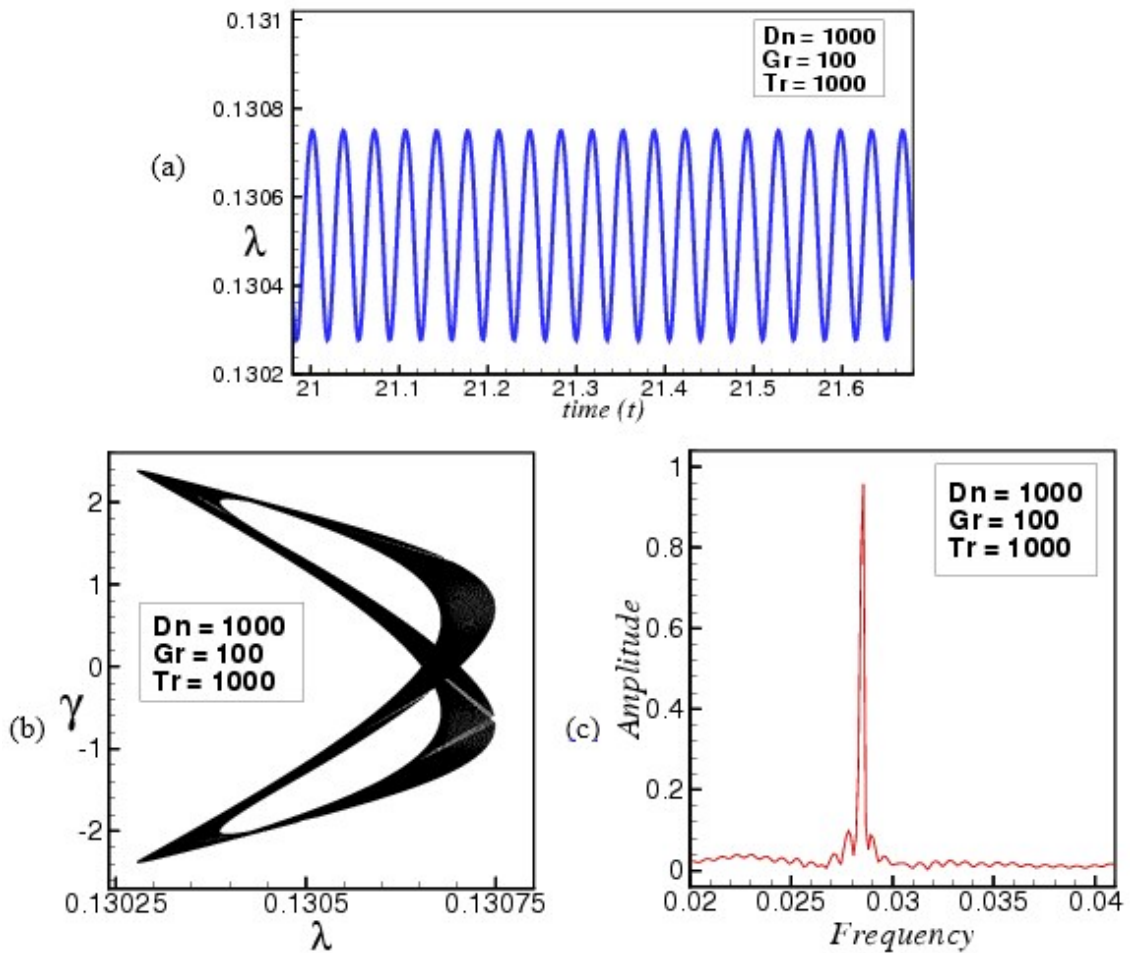


Figure 17. (a) Time dependent behavior in $t - \lambda$ plane, (b) Phase space, (c) Power spectrum, for $Tr = 1000$.

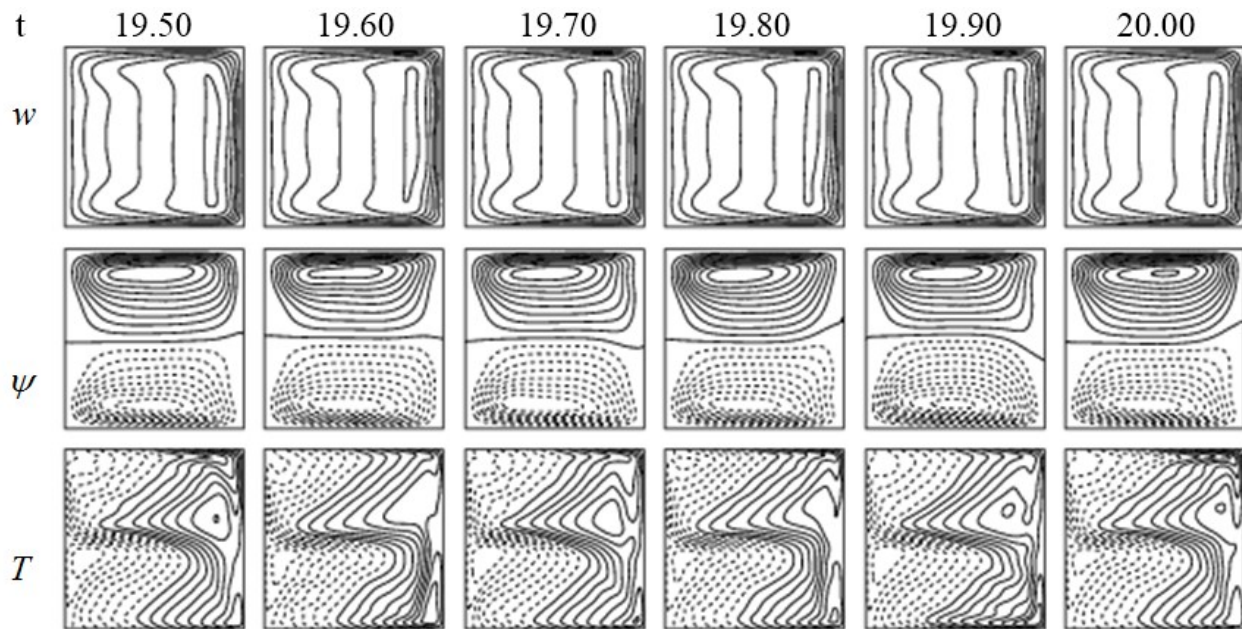


Figure 18. Contours of axial velocity (topmost), stream function (central), isotherm (lowermost) for various Dean numbers at $Tr = 1000$.

It has seen from Table 2, the steady-state solution ends at $Tr = 690.43$. When Tr is crossed over the required range, periodic oscillation has been consisted. So we have investigated the time evolution of the unsteady solutions for $Tr = 750$ and the outcomes are plotted in Figure 15 (a). It has demonstrated that the unsteady solution gives the periodic solution and this oscillation is going through $Tr = 1000$, as shown in Figure 17 (a). To ensure more, the regular oscillations have been proved with the phase space and power spectrum analysis as displayed in Figure 15 (b) & (c) and Figure 17 (a) & (b). It is explained from the power spectrum that the line spectrums have become weaker after one oscillation. It is remarked that the plane of both phase space and power spectrum is increased at $Tr = 1000$ more than $Tr = 750$ which gives an idea that the characteristics of flow behaviors are significantly affected by the Coriolis force. Two types of flow velocity axial and secondary flows and temperature profiles are shown in Figures 16 & 18. Symmetric and

asymmetric two vortex solutions are found for $Tr = 750$ & 1000 .

If the Taylor number is raised more, the periodic oscillation has shifted into multi-periodic oscillations, i.e., the multi-periodic oscillation has created at $Tr = 1250$ which has been depicted in Figure 19 (a). The phase space and power spectrum for the multi-periodic oscillation have been explored in Figure 19 (a) & (b). It is explained from the phase space and power spectrum that multiple orbits have formed in phase space plane which has crossed over each other, and the line spectrums have oscillated broadly within the frequency ranges from 0 to 0.05. Flow patterns with temperature profiles are exhibited in Figure 20. Two vortex of symmetric and asymmetric secondary flow have been created for $Tr=1250$ where the axial flow and the temperature profiles bear their usual significances. It is also depicted that from $t=15.00$ to $t=15.20$ it creates two different cycles and from $t=15.25$, it again repeats from $t=15.00$.

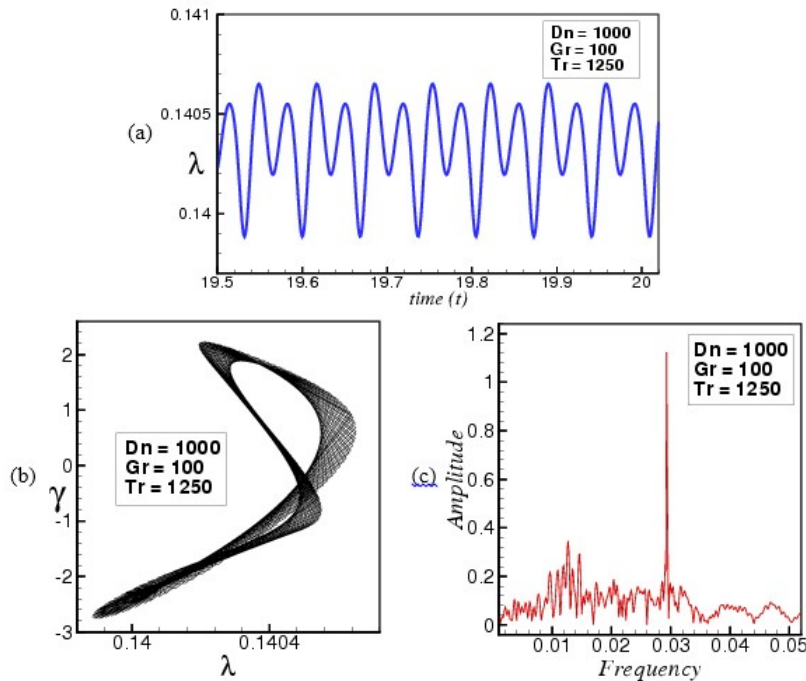


Figure 19. (a) Time dependent behavior in $t - \lambda$ plane, (b) Phase space, (c) Power spectrum, for $Tr = 0$.

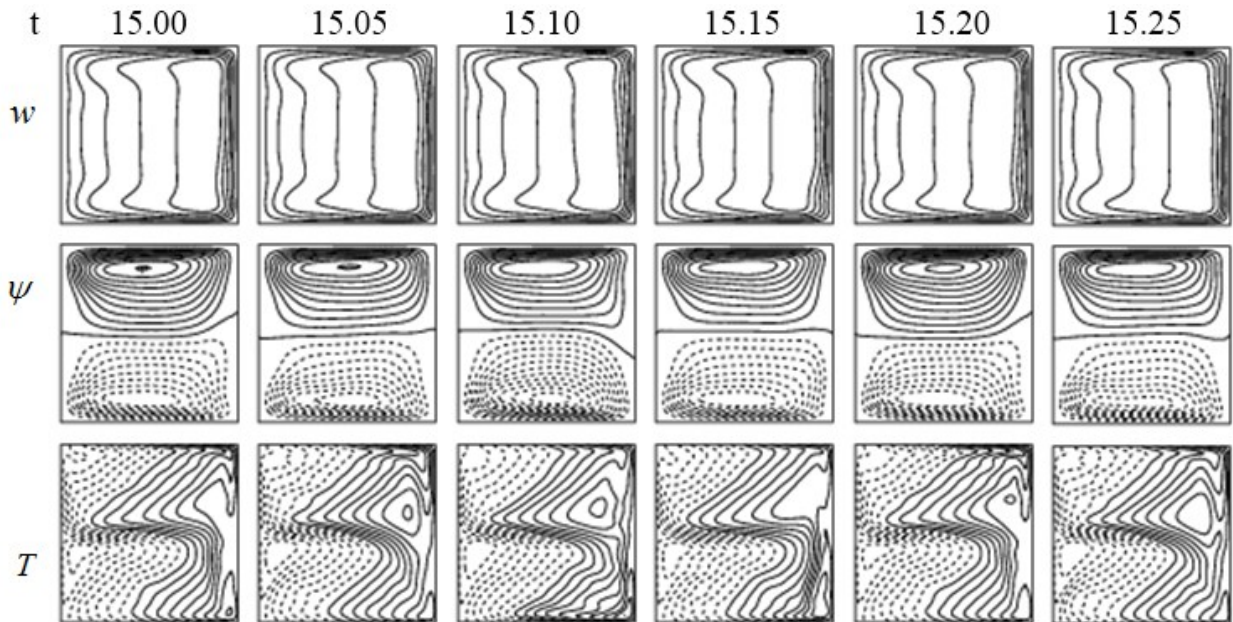


Figure 20. Contours of axial velocity (topmost), stream function (central), isotherm (lowermost) for various Dean numbers at $Tr = 0$.

Now, we have observed the time evolution calculation of the unsteady solution for $Tr = 1500$, and it is found that, at, the unsteady solution gives the chaotic oscillation which has been continued till . Figure 21 (a), 23 (b) & 25 (a) have disclosed the unsteady flow characteristics for consecutively. It has seen that the flows have oscillated more than the periodic and multi-periodic flows and the density of the oscillation has enhanced for increasing the Taylor number gradually. So the effect of the Coriolis force of the duct is easily understanding in this stage. Phase

space and power spectrum density of the chaotic oscillations are also enumerated as shown in Figure 21 (a, b), 23 (a, b) & 25 (a, b) which justifies the flow configuration as it is anticipated. From the phase space, the path lines have been passed over each other in the plane, as a result, a critical flow characterizes has been found. Power spectrum densities show that the line spectrums have vibrated continuously. It is further audited that as the Taylor number increases, the regions of the phase space and power spectrums are getting larger.

Axial flow, secondary flow and temperature profiles are depicted in Figure 22, 24 & 26 respectively. It is seen that axial flows at chaotic oscillations are more powerful than the periodic and multi-periodic oscillation. Two-, three-, four-vortex asymmetric secondary flows have created at the chaotic flow. A relationship has been also formed between the axial and secondary flow. When the axial velocity is split into two separated (upper and lower) regions along the center of the duct, it has shown four vortices where the two Dean and two Ekman vortices are

almost equal (see at). If the axial velocity of the stream moves up a little, a dumbbell is created on the bottom for which the vortex becomes large at below ($t = 18.20$ at $Tr = 1500$). The temperature profiles illustrate that the steam line of the temperature density is high when the two and four vortices have occurred. So, temperature profiles prove that the heat is transferred to the duct and the fluid absorbs the heat which is conducted by the duct wall. As a result, the fluid is an amalgamation and enhances heat transfer to the fluid.

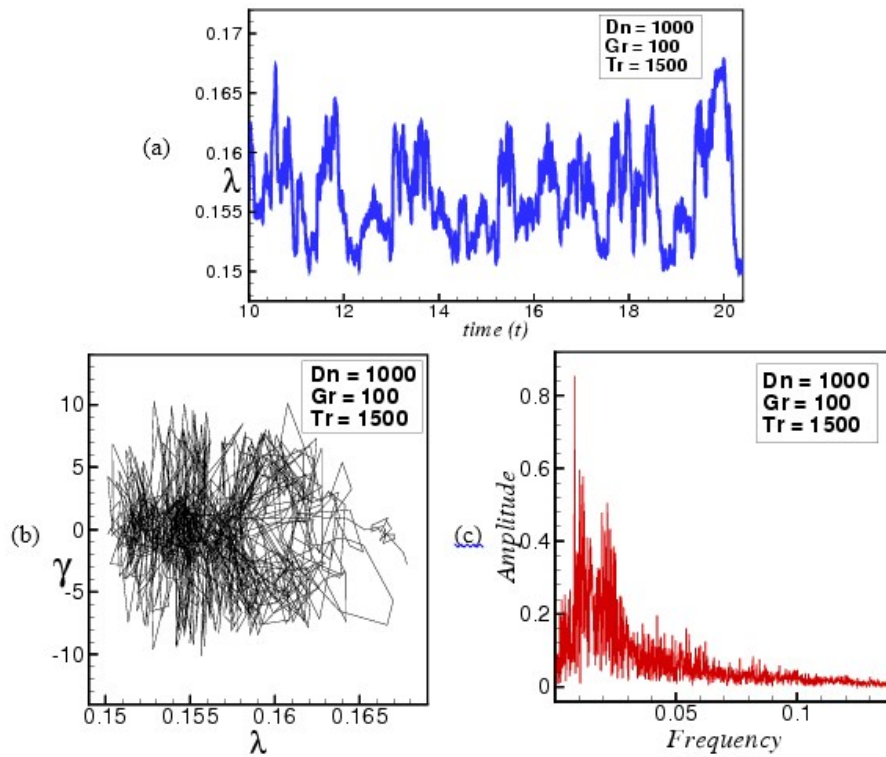


Figure 21. (a) Time dependent behavior in $t - \lambda$ plane, (b) Phase space, (c) Power spectrum, for $Tr = 1500$.

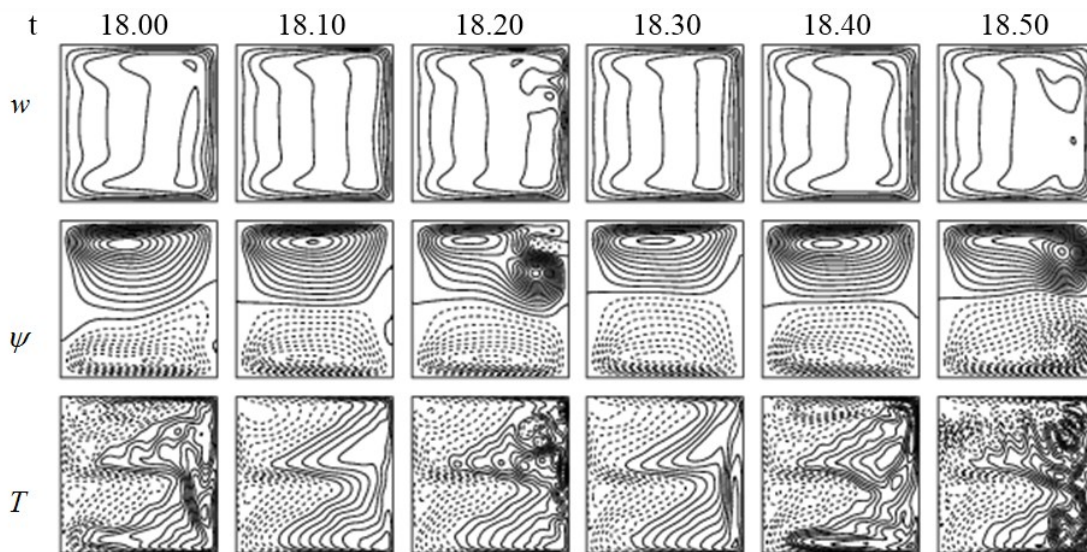


Figure 22. Contours of axial velocity (topmost), stream function (central), isotherm (lowermost) for various Dean numbers at $Tr = 1500$.

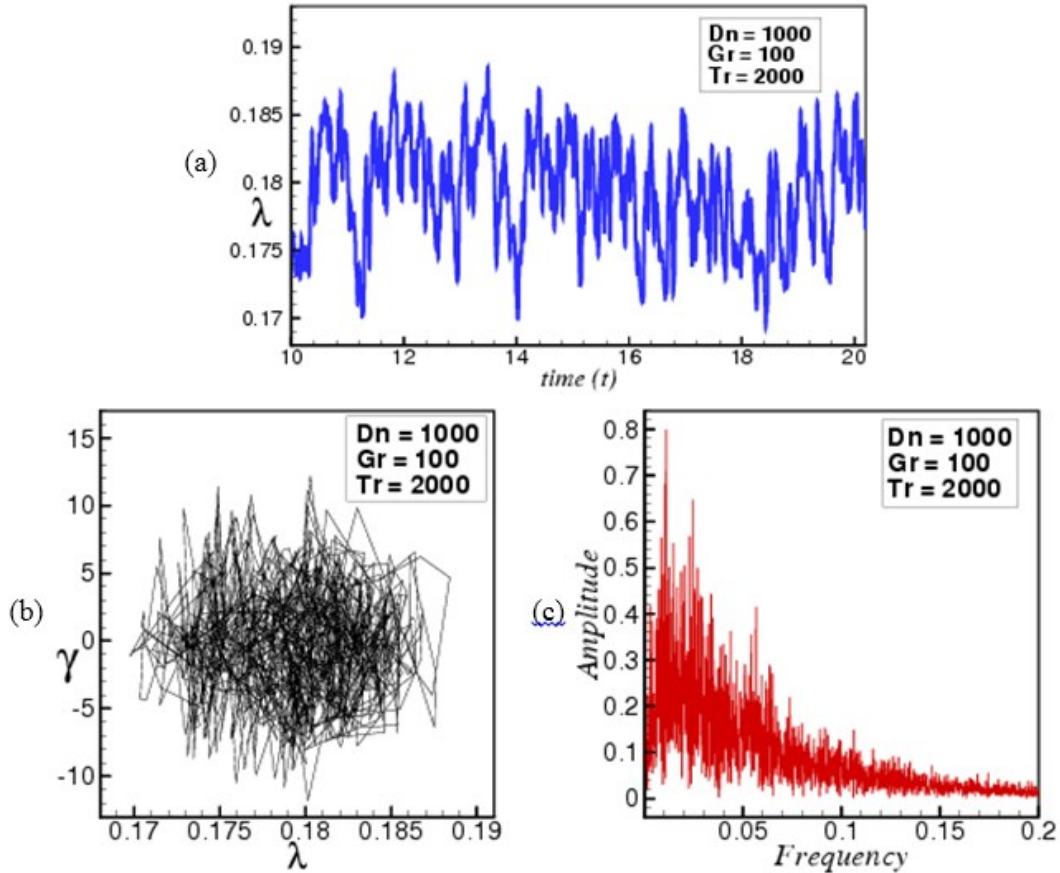


Figure 23. (a) Time dependent behavior in $t - \lambda$ plane, (b) Phase space, (c) Power spectrum, for $Tr = 2000$.

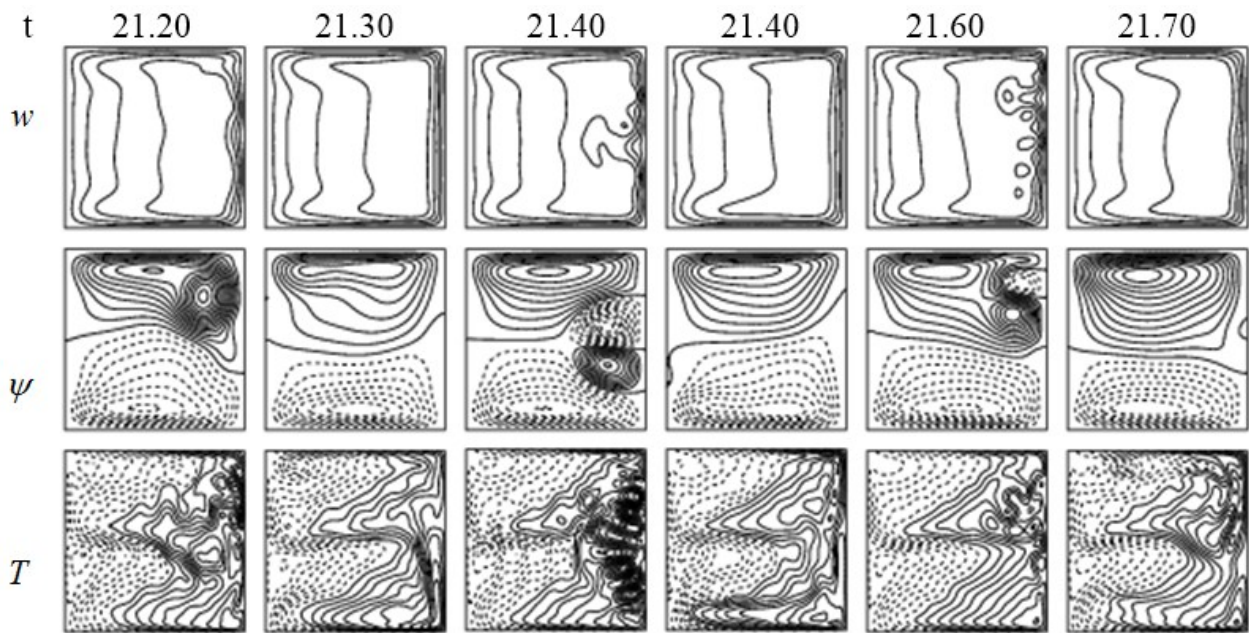


Figure 24. Contours of axial velocity (topmost), stream function (central), isotherm (lowermost) for various Dean numbers at $Tr = 2000$.

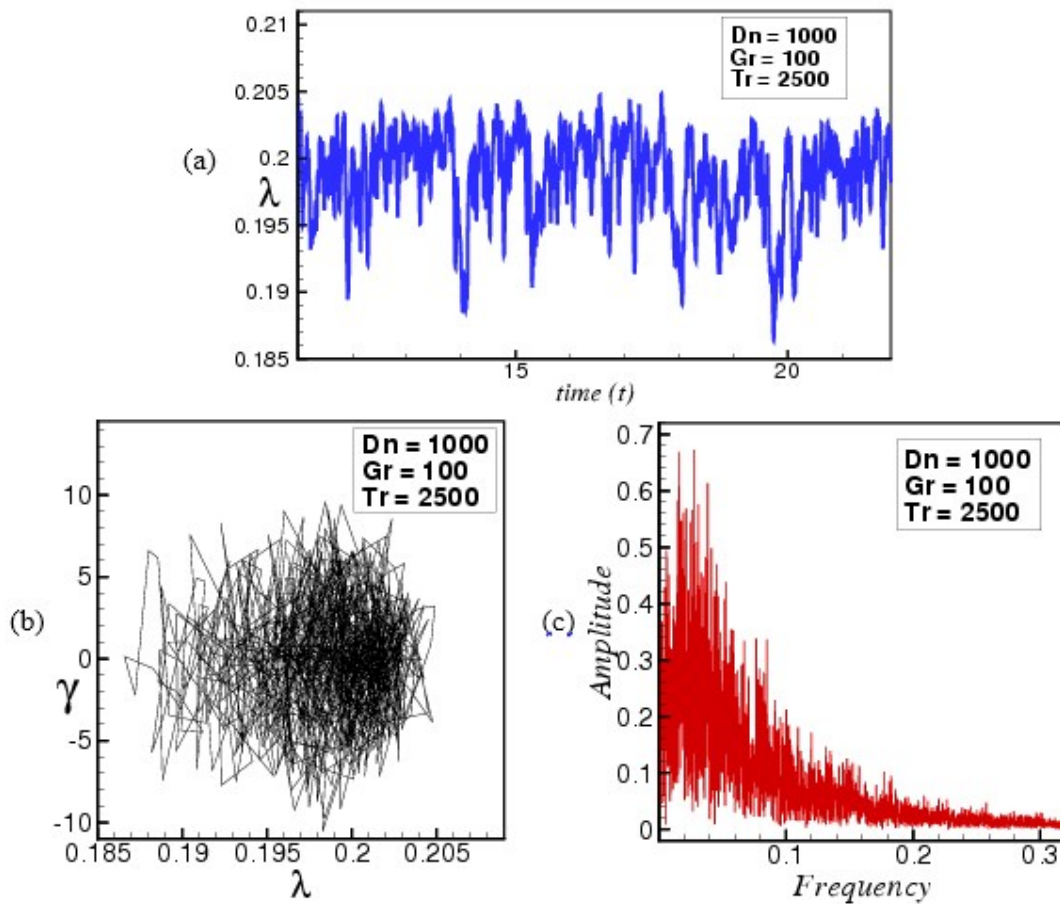


Figure 25. (a) Time dependent behavior in $t - \lambda$ plane, (b) Phase space, (c) Power spectrum, for $Tr = 2500$.

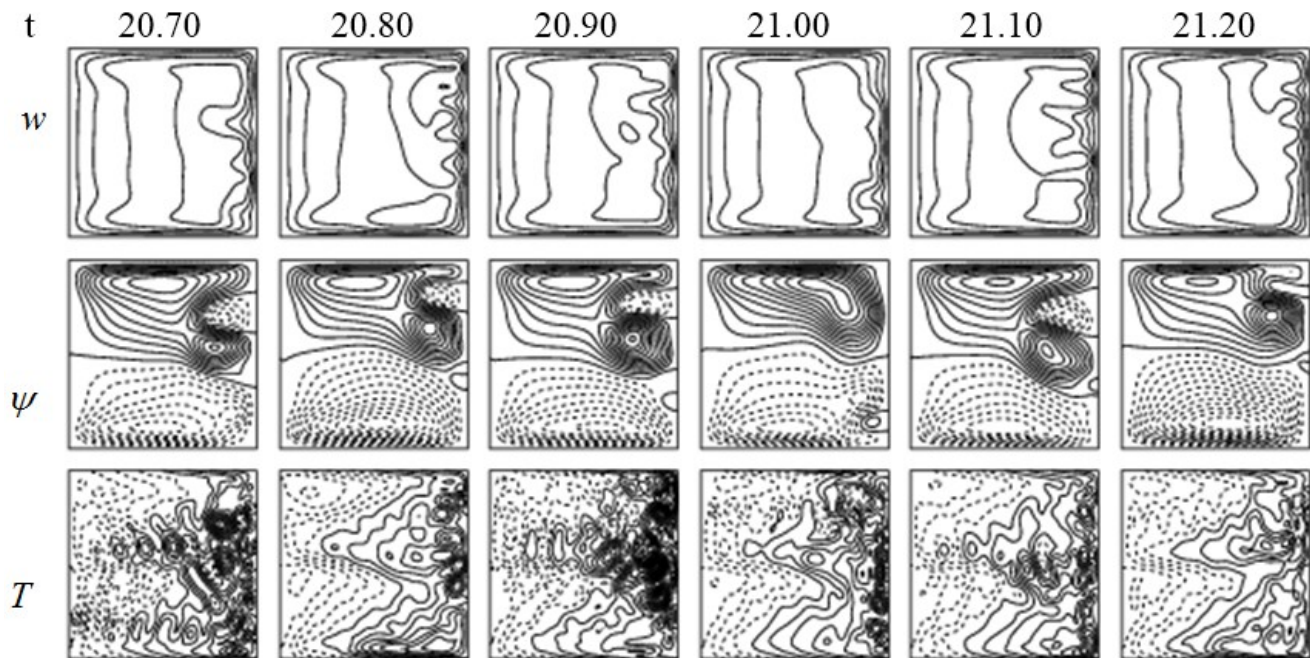


Figure 26. Contours of axial velocity (topmost), stream function (central), isotherm (lowermost) for various Dean numbers at $Tr = 2500$.

4.1.5 Vortex structures in unsteady solution for positive rotation

Here, the vortex structure of the unsteady solutions has been performed between the Taylor number, $0 \leq Tr \leq 2500$ as shown in Figure 27. Two, three, four, and five vortex have been addressed as the cross, gradient, square and left triangle. At $Tr = 0$, it shows two-, three- and four-vortex solution. From $Tr = 250$ to $Tr = 1250$, only two vortexes symmetric/asymmetric to vortex solutions have been found and from $Tr = 1500$ to $Tr = 2500$, two-, three-, four-vortex have been originated in the curved square duct. It is described that the number of vortex and heat transfer at multi-periodic and chaotic oscillation is more than that on the steady-state and periodic oscillation.

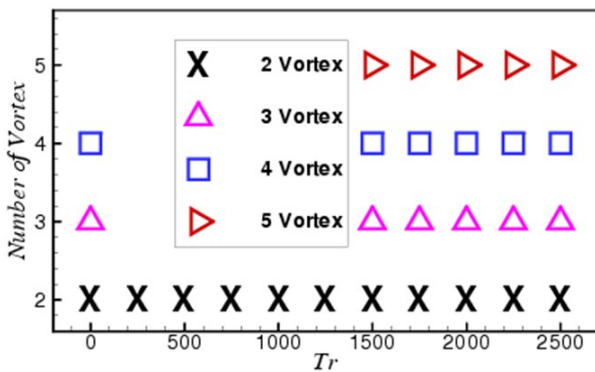


Figure 27. Vortex structures of the unsteady solution branches for several Taylor numbers ($0 \leq Tr \leq 2500$).

4.1.6 Temperature Gradients

To investigate the transfer of heat at the cooled and heated sidewalls of the fluid, temperature gradients have been computed, which have been sketched in Figure 28. It can be said from the cooled sidewall (Figure 28 (a)) that the heat has risen gradually in the central region for increasing the Taylor number after some ups and downs at both sides. This has happened due to the bend on the duct. On the other hand, temperature gradients for heated sidewall (Figure 28 (b)) have demonstrated that the transfer of heat has climbed at the opposite side of the center and subsequently decreasing in the central region. This is caused because of the curvature of the duct around $y = 0$, which has also affected the secondary flow structures. So the inquiry not only revealed the temperature gradients but also build up a bond between the secondary flow and the fluid mixing.

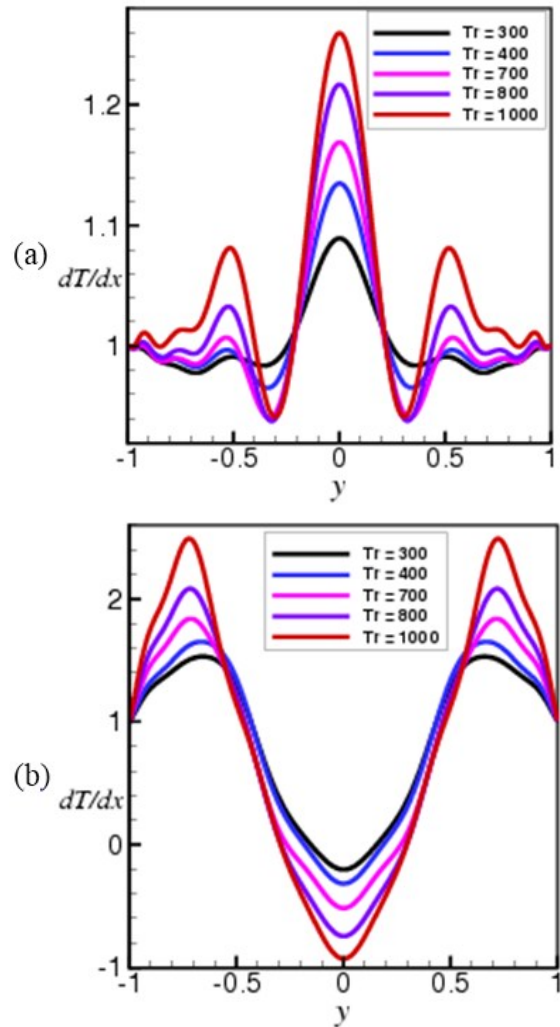


Figure 28. Temperature gradients for several Taylor numbers and $\delta = 0.01$, (a) cooled side walls, (b) heated side walls.

4.2 Negative Rotation

4.2.1 Linear Stability analysis

Linear stability for the negative rotation with different Taylor number ($-10 \leq Tr \leq -2500$) has been calculated in this section. Table 3 has explained the stability analysis. It is demonstrated that the stability analysis shows the unstable region throughout the range of Taylor number except $-160.00 \leq Tr \leq -374.46$ and $-633.88 \leq Tr \leq -867.32$. Here, the stable regions in Table 3 are addressed with italic sign where the consecutive stable and unstable points are designated by bold sign.

Table 3. Stability analysis for the curved duct between $-10 \leq Tr \leq -2500$

Tr	λ	σ_r	σ_i	Criteria
-10	0.04187942694224612	1.3393×10^1	2.5489×10^1	Linear Unstable
-159.99	0.05415345492572633	1.0301×10^1	0	Linear Unstable
-160.00	0.05455372420640438	-5.2402×10^{-1}	0	Linear Stable
-250	0.06511878029113763	-1.4485	0	Linear stable
-374.46	0.07441477982680612	-1.0959	0	Linear stable
-374.47	0.07448794933147594	4.1831	0	Linear Unstable
-500	0.08714241004390948	1.0818	2.1873×10^1	Linear Unstable
-633.87	0.09164829460364005	.074534	1.4658×10^1	Linear Unstable
-633.88	0.09164925456387563	-1.0623	0	Linear stable
-750	0.1042801087783404	-4.78126	0	Linear stable
-867.32	0.10846037936452035	-.097354	0	Linear stable
-867.33	0.10846562439564629	1.34342×10^1	-1.465×10^1	Linear Unstable
-1000	0.1174137857313870	7.3338×10^1	-3.7178×10^1	Linear Unstable
-1250	0.1288555049676210	9.2333×10^1	4.7812×10^1	Linear Unstable
-1500	0.1391208989343701	1.0705×10^2	-5.6219×10^1	Linear Unstable
-2000	0.1574690862841000	1.2790×10^2	-6.9668×10^1	Linear Unstable
-2500	0.1740364752924417	1.3999×10^2	8.1321×10^1	Linear Unstable

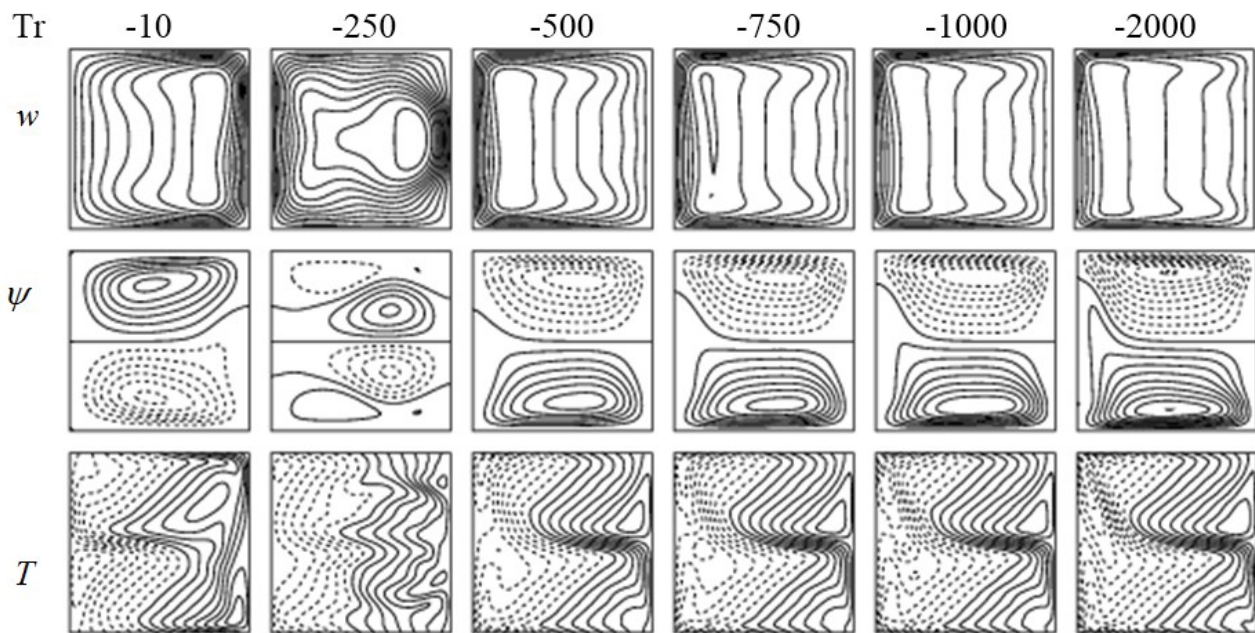


Figure 29. Contours of axial velocity (topmost), stream function (central), isotherm (lowermost) for various Taylor numbers.

Flow velocity such as axial and secondary flows and the temperature profiles are displayed in Figure 29. From $Tr = -10$ to $Tr = -250$, the axial velocity has pushed to the inner wall of the duct where this velocity acts as reverse from $tr = -500$ to $Tr = -2500$. Secondary velocity shows that without $Tr = -250$, the other Taylor numbers have generated only two-vortex asymmetric flow. In the unsteady flow analysis, the two vortex solutions have also consisted of three-, four-, five-vortex at the irregular oscillation which is discussed in the time evolution calculation of the unsteady solution section. It

is also seen that the dotted lines of the secondary flows are formed at the upper wall of the duct. This is generated due to the negative rotation and the dominance of the curvature.

4.2.2 Time evolution calculations

Now, the unsteady flow characteristics of negative rotation have been pursued for different Taylor number $-10 \leq Tr \leq -2500$ with a fixed difference of Taylor number 250.

For $Tr = -10$, we have accomplished the time evolution calculation of the unsteady solution and it represents the multi-periodic oscillation which is shown in Figure 30 (a). To explain the multi-periodic oscillation more evidently, phase space and power spectrums are plotted in Figure 30 (b) & (c). From the phase space, the way lines are met at the starting point after completing two cycles. The power spectrums are demonstrated that the line spectrums are weaker through the strong frequencies. Two types of flow velocity such as axial and secondary flows and their temperature profiles have been exhibited in Figure 31. Axial flow patterns describe us that, when two vortex asymmetric solutions have consisted it is only

pushed at the outer wall of the duct ($t = 19.30$). The axial velocity also forms a dumbbell at the outer wall of the duct at $t = 18.90$ and as a consequence, another vortex has appeared in the lower part of the duct. At time $t = 19.10$, two high-velocity regions have been constructed, so the flow velocity has much higher than $t = 18.90$ & 19.00 ; has fully formed four vortex solution. The dumbbells of the axial velocity have reduced from the upper and outer wall at $t = 19.20$ with containing the two high-velocity regions. Because of the axial velocity properties, the Ekman vortices at the lower side are larger than the upper side. This is almost same as the positive rotation of the duct for $Tr = 0$ at $t = 20.40$.

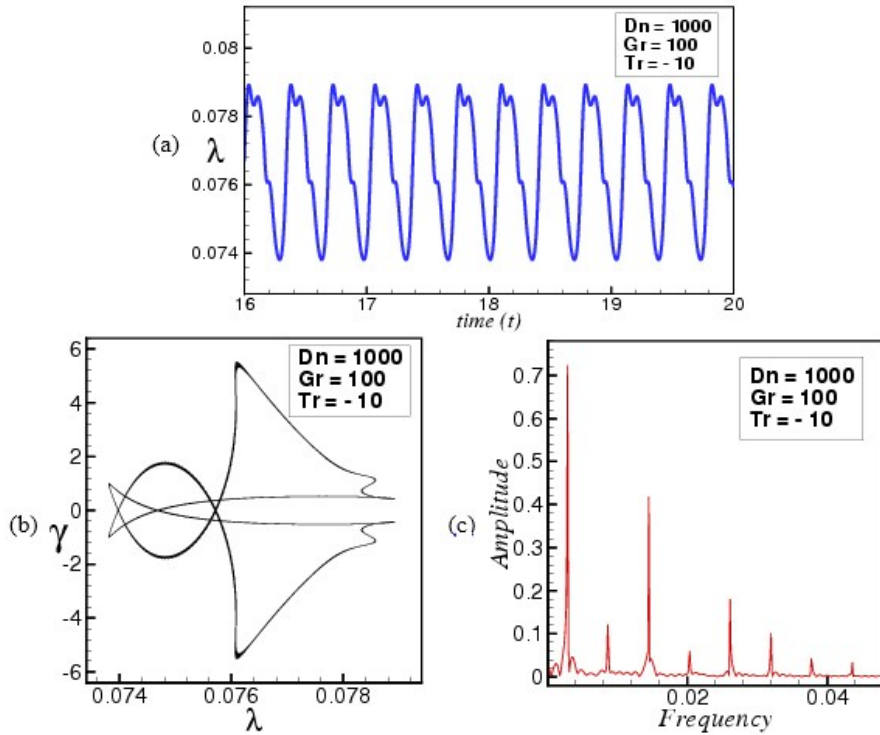


Figure 30. (a) Time dependent behavior in $t - \lambda$ plane, (b) Phase space, (c) Power spectrum, for $Tr = -10$.

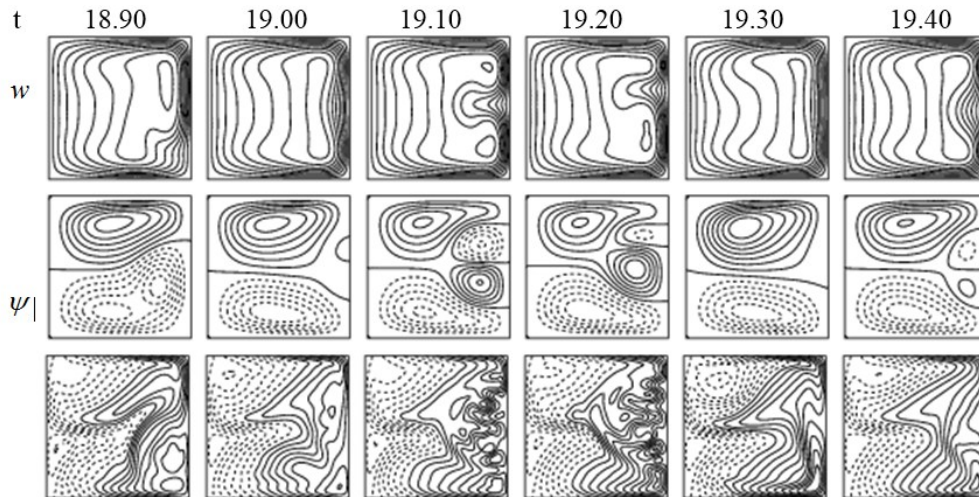


Figure 31. Contours of axial velocity (topmost), stream function (central), isotherm (lowermost) for various Dean numbers at $Tr = -10$.

If the Taylor number has increased in the negative direction, the unsteady solutions are converted into steady-state oscillations. The steady-state oscillations are initiated from $Tr = 160.00$ which is found from the linear stability analysis. Figure 32 (a) displays the steady-

state solution at $Tr = -250$. Flow characteristics (axial and secondary) and temperature profiles are visualized in Figure 32 (b). Six vortex symmetric secondary vortices have been originated For the steady-state solution.

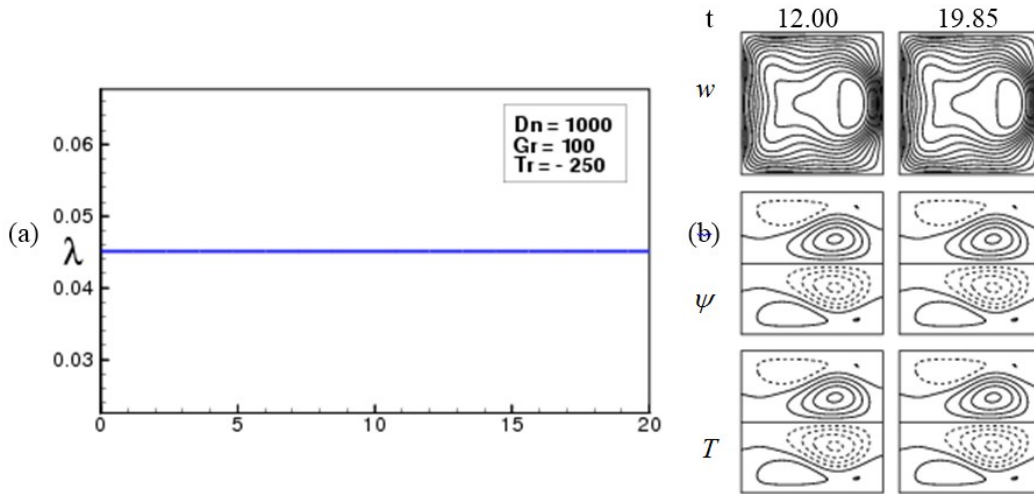


Figure 32. (a) Time dependent behavior in $t - \lambda$ plane, (b) Contours of axial velocity (topmost), stream function (central), isotherm (lowermost) for various Dean numbers at $Tr = -250$.

If the Taylor number is increased further, the steady-state solution is turned into multi-periodic oscillation at $Tr = -500$ as shown in Figure 33 (a). The phase space and power spectrum are also exposed in Figure 33 (b) & (c), which demonstrated that the path lines are consisted of two multiple orbits before meeting with the starting points, and the line spectrums become weaker after exceeding 0.5 on the frequency line. Two types of flow velocity axial and secondary flows and temperature profiles are revealed in Figure 34. It is said that interesting types of flow properties have been found for . From the axial flow, the flow velocity has pushed at the outer wall of the duct. The secondary vortices of the flow patterns

depict that due to the Coriolis force in the negative direction the dotted lines are produced at the upper wall of the duct and the solid lines are created at the lower wall of the duct. As a consequence of these types of rotation of negatively, the Ekman vortices have originated at the inner wall of the duct. At time , two high-velocity regions are formed at the inner side of the duct walls and these high-velocity regions are affected the secondary flow and two new Ekman vortices appear. At time , the dumbbells consist at the lower side of the inner wall, so the dividing streams lines are moved on the upper side, so the vortices at the lower portion are bigger than the upper vortices.

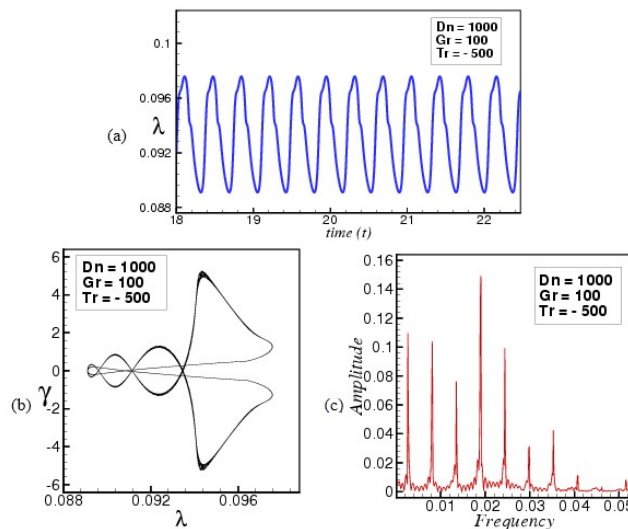


Figure 33. (a) Time dependent behavior in $t - \lambda$ plane, (b) Phase space, (c) Power spectrum, for $Tr = -500$.

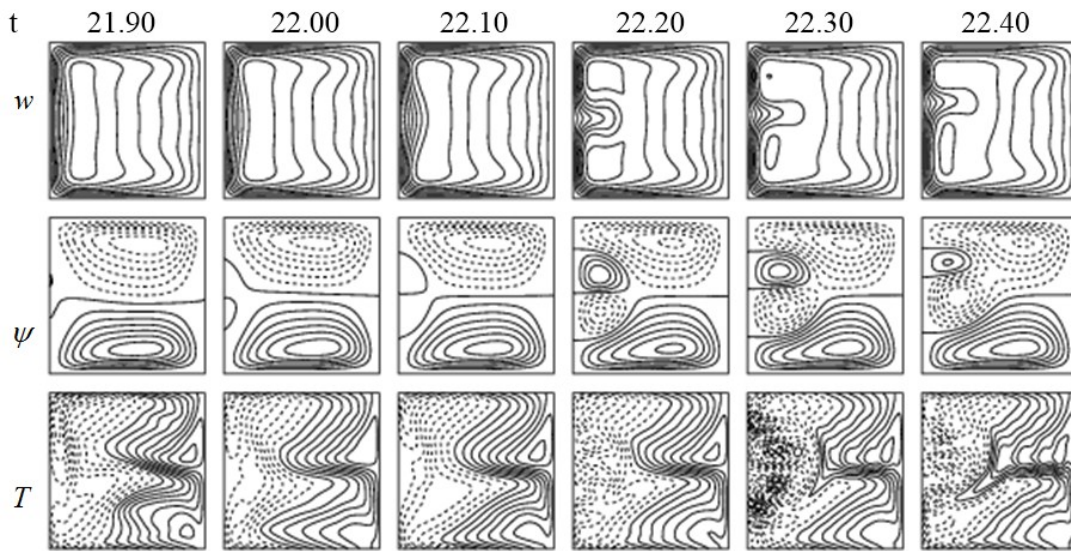


Figure 34. Contours of axial velocity (topmost), stream function (central), isotherm (lowermost) for various Dean numbers at $Tr = -500$.

Now, we have manifested time evolution calculation of the unsteady solution for $Tr = -750$, and it has found that the unsteady solution gives steady-state solution as shown

in Figure 35 (a). The unsteady solution at is also justified by the linear stability analysis. Axial flow, symmetric secondary flow, and temperature profiles are explored in Figure 35 (b).

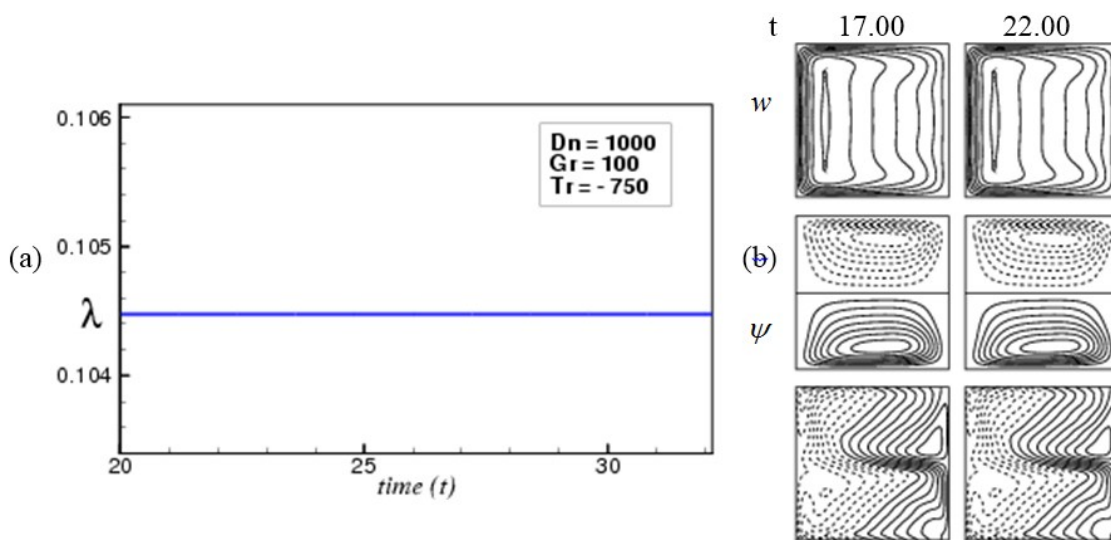


Figure 35. (a) Time dependent behavior in $t - \lambda$ plane, (b) Contours of axial velocity (topmost), stream function (central), isotherm (lowermost) for various Dean numbers at $Tr = -750$.

If the Coriolis force is raised in the negative direction, the steady-state solution has switched to the periodic oscillation from $Tr = -867.33$ and it has continued up to $Tr = -1350$. Time evolution results for $Tr = -1000$ & -1250 have displayed in Figures 36 (a) & 38 (a) respectively. To be clear more about the regular oscillation, phase spaces and power spectrums have also drawn in Figure 36 (b, c) & 38 (b, c). Phase spaces deliberate that the paths are meet at the starting point after completing an orbit. Power spectrums demonstrated that the line spectrums and its harmonics are seen which

allude that the flow is a periodic solution. Apparently phase space and power spectrum seem to have some differences between $Tr = -1000$ and $Tr = -1250$. The regions of the phase space and power spectrum are enhanced for increasing Taylor numbers gradually. This is befallen because of the Coriolis force. Two types of flow patterns axial and secondary flows, and the temperature profiles are shown in Figure 37 & 39. Two vortex asymmetric flow patterns are formed for $Tr = -1000$ & -1250 .

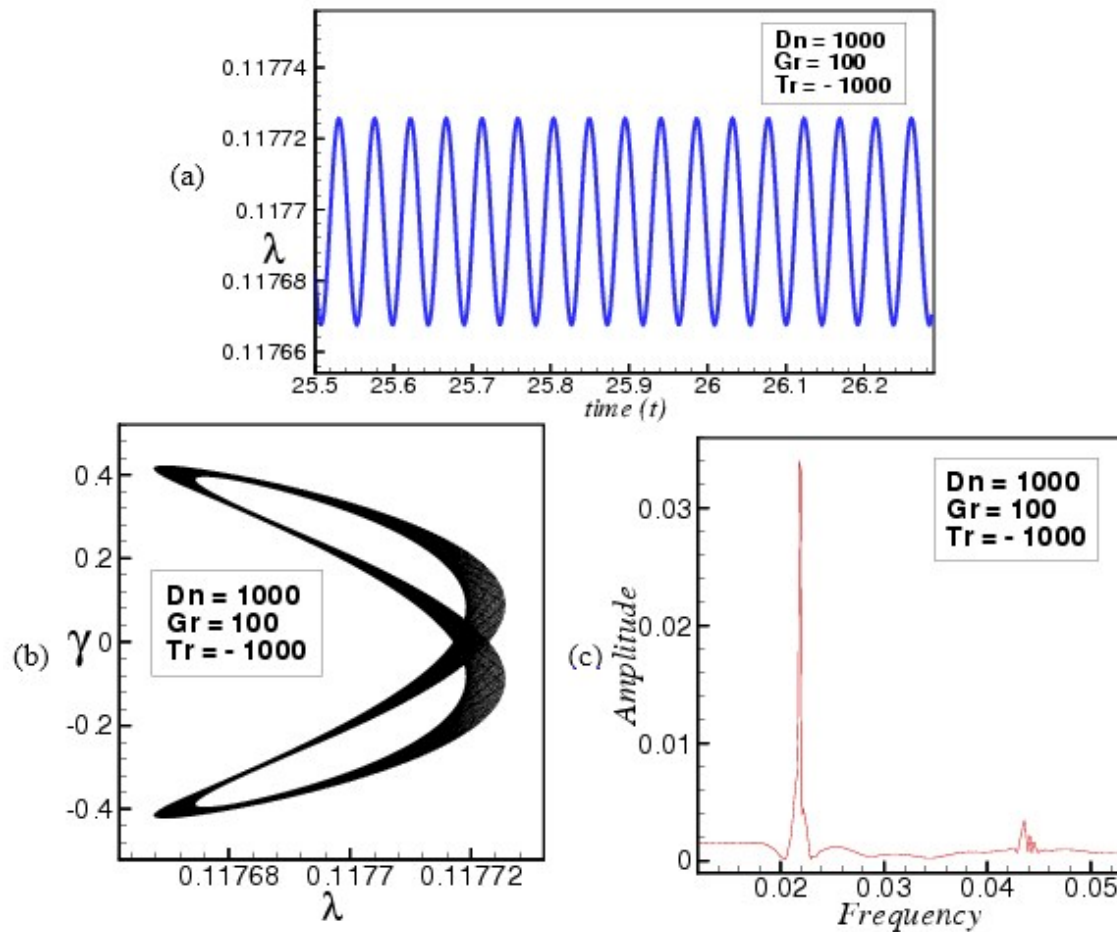


Figure 36. (a) Time dependent behavior in $t - \lambda$ plane, (b) Phase space, (c) Power spectrum, for $Tr = -1000$.

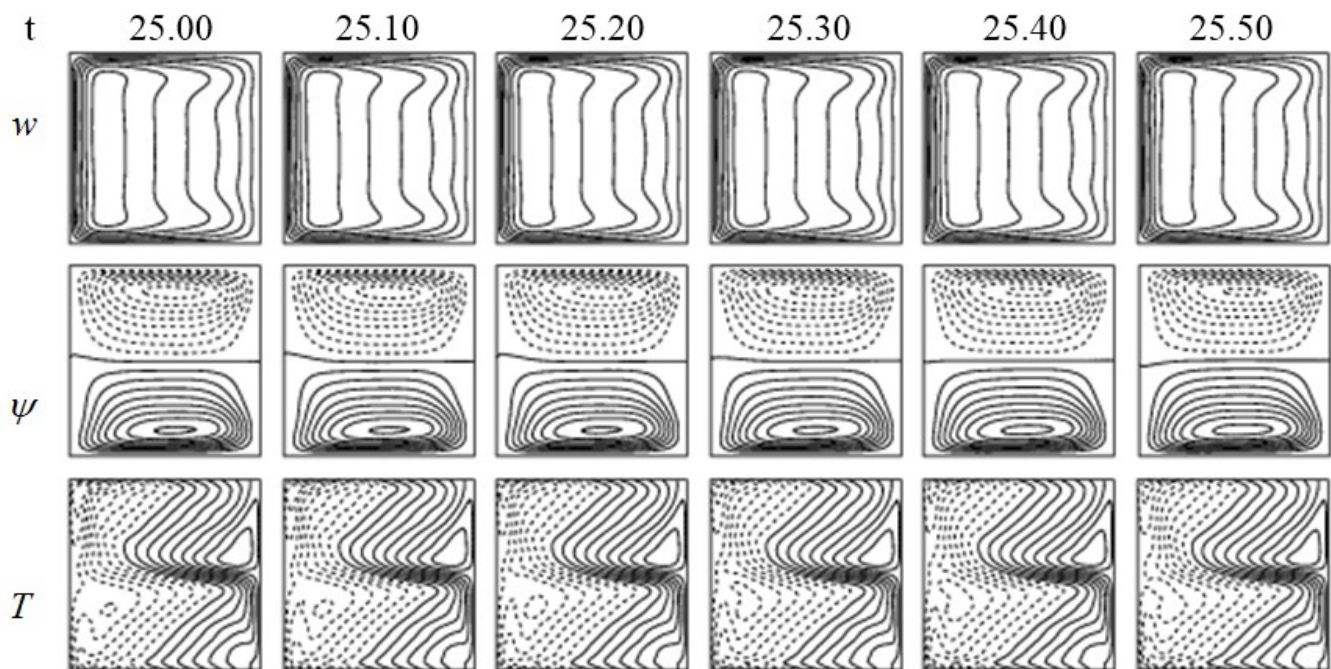


Figure 37. Contours of axial velocity (topmost), stream function (central), isotherm (lowermost) for various Dean numbers at $Tr = -1000$.

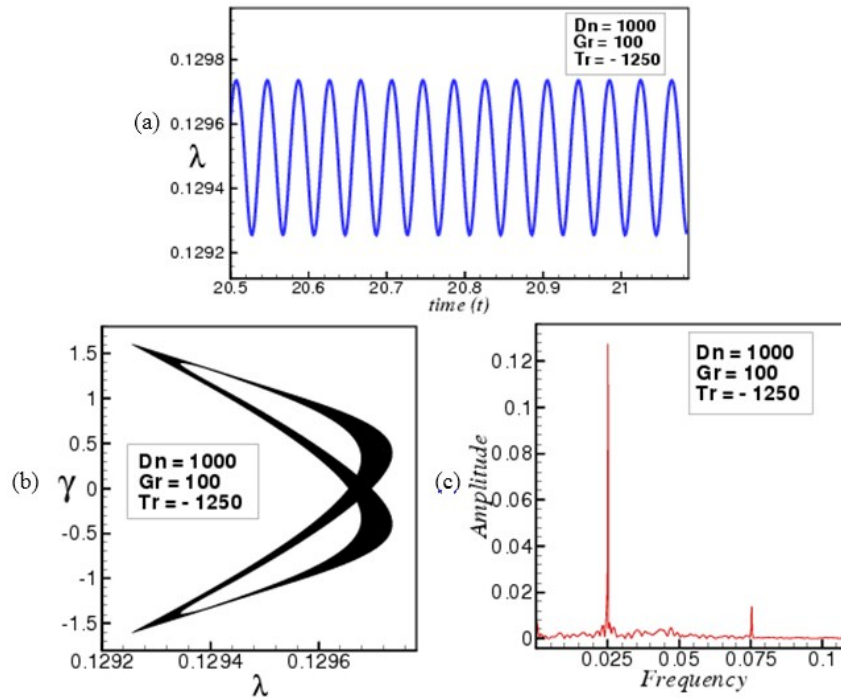


Figure 38. (a) Time dependent behavior in $t - \lambda$ plane, (b) Phase space, (c) Power spectrum, for $Tr = -1250$.

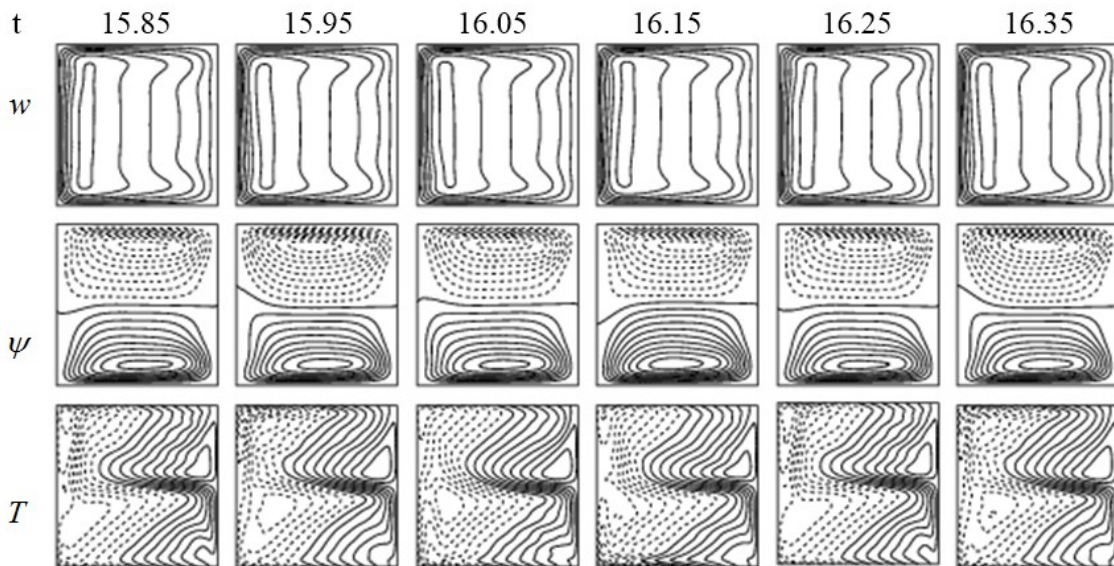


Figure 39. Contours of axial velocity (topmost), stream function (central), isotherm (lowermost) for various Dean numbers at $Tr = -1250$.

Here, we have also explored unsteady investigations from $Tr = -1500$ to $Tr = -2500$. It has demonstrated that the unsteady solution delivers chaotic oscillation between the required range of Taylor number. Figure 40 (a), 42 (a) and 44 (a) show the chaotic oscillation for $Tr = -1500, -2000, -2500$ respectively. To have a clear insight into the flow, phase space and power spectrums are also calculated and depicts in Figures 40 (b, c), 42 (b, c) and 44 (b, c). Phase space and power spectrum are narrated that the path of the stream flow is moved willingly in the $\lambda - \gamma$ plane, and the line spectrums oscillate continuously.

It has also seen that the area of both phase space and power spectrums has risen up for increasing Taylor number gradually. Axial flow, secondary flow, and temperature profiles are shown in Figures 41, 42 and 45. Two, three and four vortex solutions are found for $Tr = -1500, -2000, -2500$ where the dotted lines are seen in the upper wall of the duct and the additional vortices are situated in the inner wall of the duct. At $t = 14.40$ of $Tr = -1500$, axial flow regions are created from below, so the secondary vortices are consisted of below. On the other hand, at $t = 15.30$, flows are occurred reversely, so

the additional vortices are formed from above. When the four vortex solutions are found the axial flows are divided into two high-velocity regions and the fluid are mixed up more than that of the two vortex solution which is also

seen by the temperature profiles. So the unsteady solutions do not demonstrate only the time-dependent solutions but also disclose a connection between the liner stability, axial flows, secondary flows and the heat transfer.

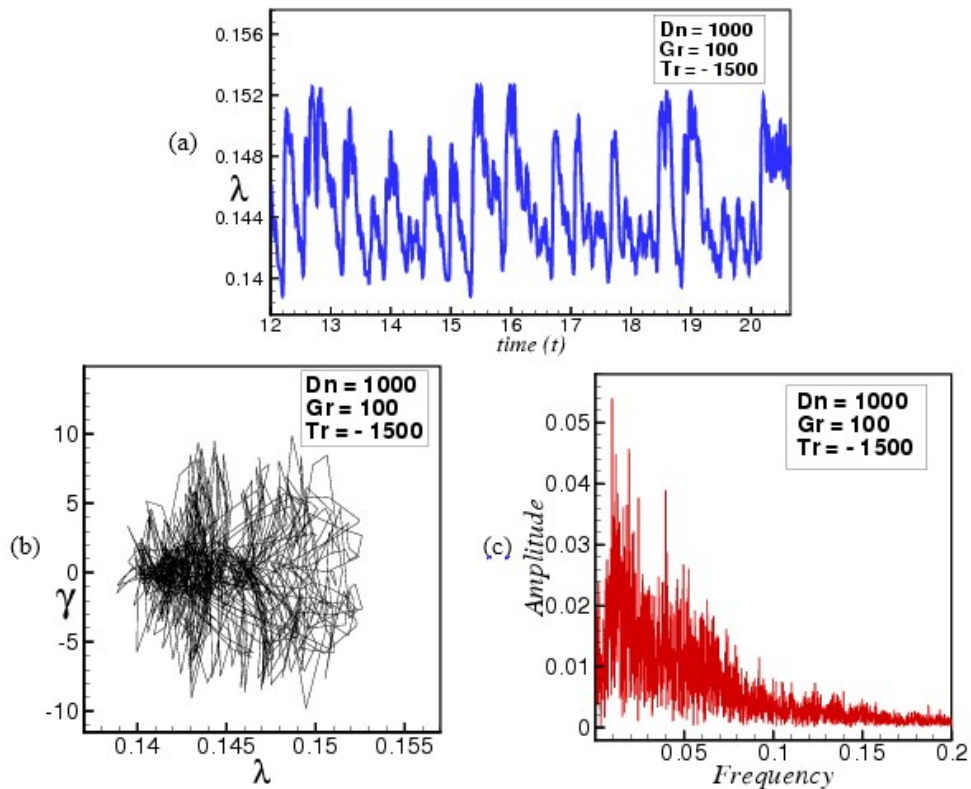


Figure 40. (a) Time dependent behavior in $t-\lambda$ plane, (b) Phase space, (c) Power spectrum, for $Tr = -1500$.

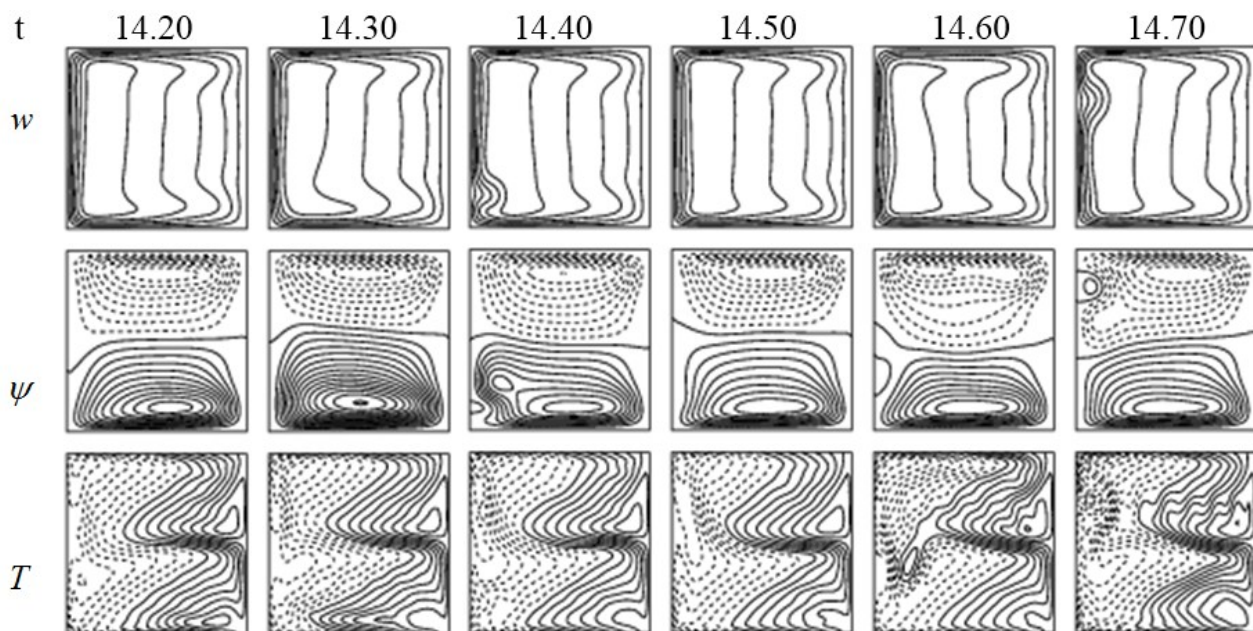


Figure 41. Contours of axial velocity (topmost), stream function (central), isotherm (lowermost) for various Dean numbers at $Tr = -1500$.

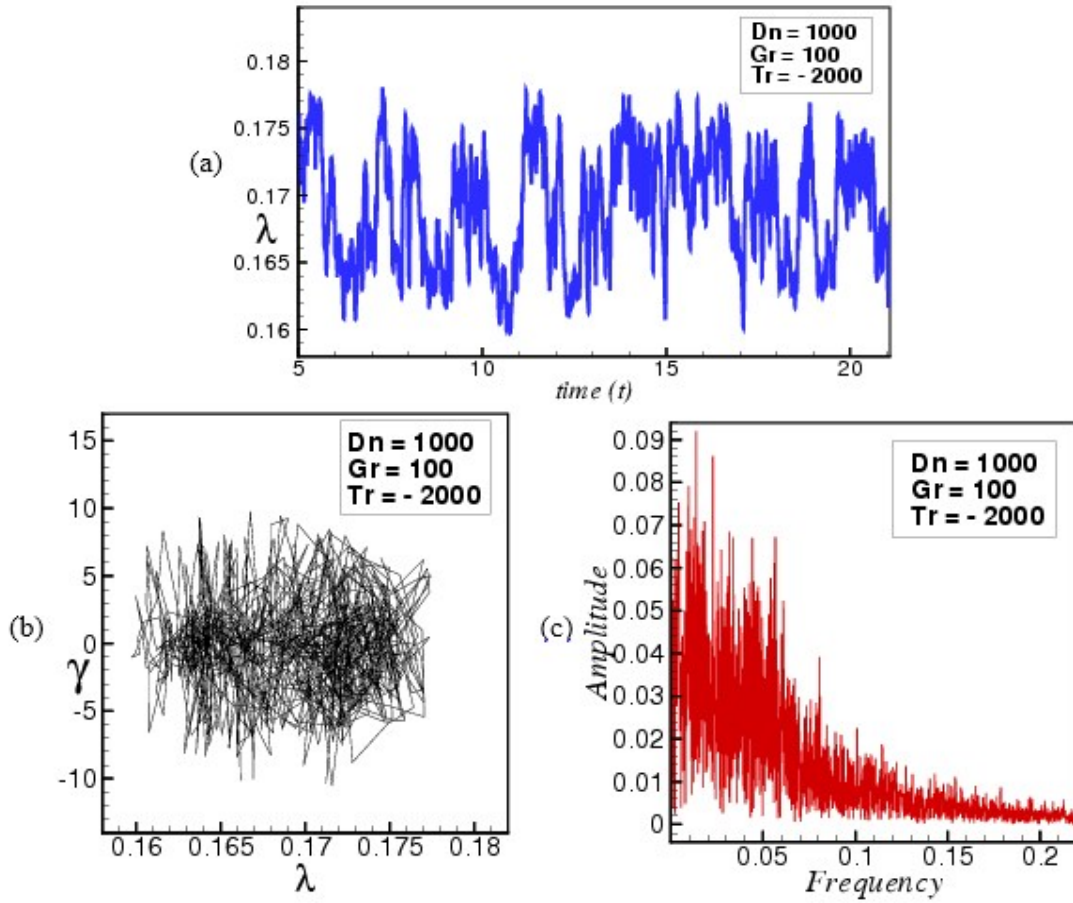


Figure 42. (a) Time dependent behavior in $t - \lambda$ plane, (b) Phase space, (c) Power spectrum, for $Tr = -2000$.

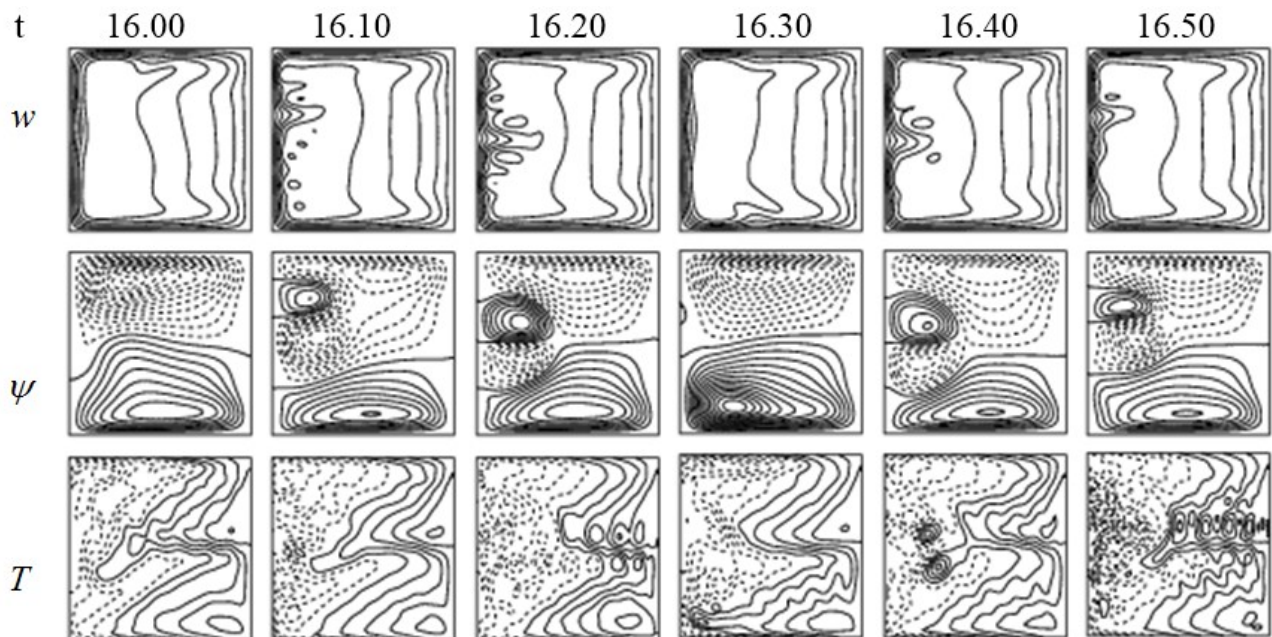


Figure 43. Contours of axial velocity (topmost), stream function (central), isotherm (lowermost) for various Dean numbers at $Tr = -2000$.

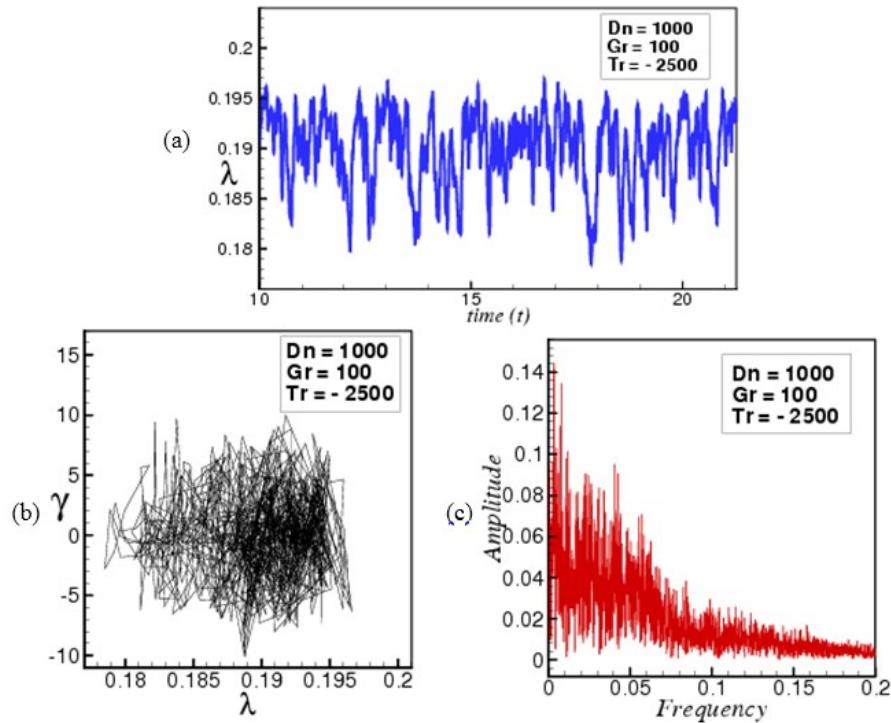


Figure 44. (a) Time dependent behavior in $t - \lambda$ plane, (b) Phase space, (c) Power spectrum, for $Tr = -2500$.

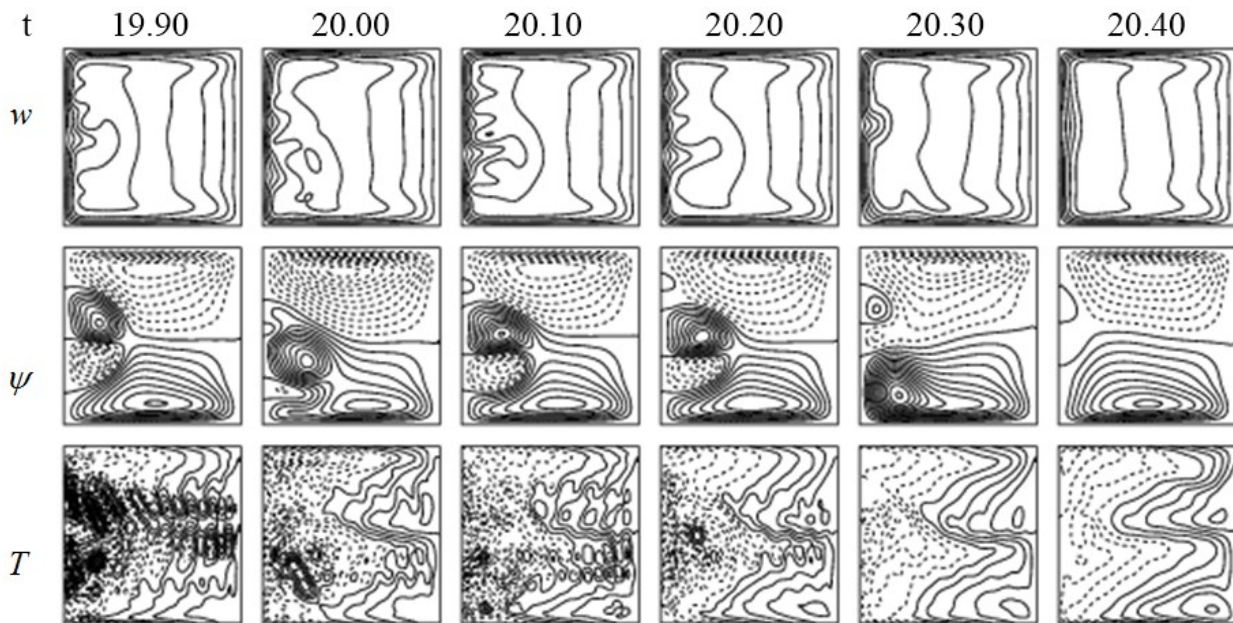


Figure 45. Contours of axial velocity (topmost), stream function (central), isotherm (lowermost) for various Dean numbers at $Tr = 2500$.

4.2.3 Vortex structures in unsteady solution for negative rotation

Constitutions of the number of the vortex through the curved square duct of negative rotation have been performed in the “ Tr vs. Number of Vortex” plane between $-10 \leq Tr \leq -2500$ with a fixed difference 250. Here, we see from Figure 46 that two vortex symmetric/asymmetric

solutions are created for steady-state and periodic oscillation; two up to four vortex are found for multi-periodic and transitional chaotic oscillation, and two up to five vortex solutions have consisted for strong chaotic oscillation. It is noted that only six vortex solution has been found for the steady-state solution at $Tr = -250$. So this section described that the fluid is mixed at the multi-

periodic and chaotic oscillation more than that on the steady-state and periodic oscillation. As a consequence, the heat transfer in the fluid at steady-state and periodic has fewer than the multi-periodic and chaotic oscillation.

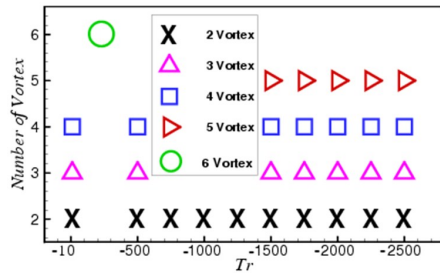


Figure 46. Vortex structures of the unsteady solution branches for several Taylor numbers ($-10 \leq Tr \leq -2500$).

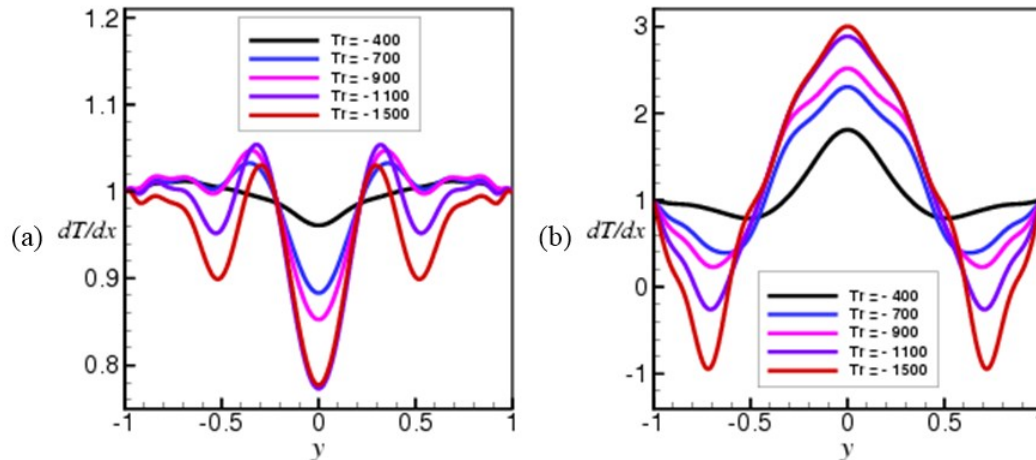


Figure 47. Temperature gradients for several Taylor numbers and $\delta = 0.01$, (a) Cooled side walls, (b) Heated side walls.

5. CONCLUDING REMARKS

Two-dimensional numerical analysis on the curved duct flow has been performed in the current study. Investigations have been carried out for specific Dean number, $Dn = 1000$; Grashof number, $Gr = 100$; curvature, $\delta = 0.01$; and a broad range of Taylor number, $-2500 \leq Tr \leq 2500$. Here, the works on positive and negative rotations have been executed individually. For positive rotation, two steady solution branches are found where there is no bifurcation relationship among them. The first branch has no limit points where the second steady branch has lots of turnings within the range of Taylor number. Linear stabilities have been also accomplished for both positive and negative rotation. It is found that among the two steady branches, linear stable points have existed within a small region of the second branch. Time evolution of the unsteady solution is then calculated for different rotational numbers. A relationship has been found between the linear stability and unsteady solutions. It is narrated that the unsteady solutions undergo various flow instabilities for both positive and negative rotation. The unsteady flow instabilities are addressed as “multi-periodic \rightarrow steady state periodic multi-periodic chaotic” for positive rotation and “multi-

4.2.4 Temperature Gradients

Here, the temperature gradients of the cooled and heated sidewalls for negative rotation are shown in Figure 47. It is described from Figure 47 (a) for cooled sidewall that the heat has descended gradually at the central region for increasing the Taylor number after some down and up at both sides. On the contrary, temperature gradients for heated sidewall have explored (Figure 47 (b)) that the transfer of heat has fallen down at the opposite side of the center and subsequently increase in the central region. It is significant that the characteristics of temperature gradients at negative rotation behave totally opposite to the positive rotation. This is happened because of the effect of the rotational parameter.

periodic steady state multi-periodic steady state periodic chaotic.” It has seen that the flow characteristics have changed at negative rotation fewer than that on the positive rotation. To be evident more about regular and irregular oscillation, phase space and power spectrums are also obtained. It is said from the analysis that the size of the phase space and power spectrum plane raises for increasing Taylor number. So it is obvious that the creation of the regular and irregular oscillations at the low rotations is weaker than the high rotations of the duct. Two types of flow velocity such as axial and the secondary flow and their temperature profiles have been also explored for different rotational parameters. Two up to eight vortex solutions have been found for both steady solution branches and unsteady solutions. For steady solution branches, it has demonstrated the structural change of secondary flow in the turning points. On the other hand, only two vortex solutions have been consisted of the steady-state solution and two up to eight vortexes have been built for periodic, multi-periodic and chaotic flows. A connection among the axial and the secondary flow has been established for the regular and irregular oscillation which also satisfies the temperature profiles. Moreover, Vortex diagrams have revealed about the fluid mixing and the transmission of

the heat through the duct. Temperature gradients show that the heat has been continuously passing from fluid particle and the wall of the duct and it has been rising up for increasing the rotation of the duct for positive and negative direction. The existent report also describes that a strong dominance among the forces (heating buoyancy, centrifugal and Coriolis) in the rotating duct that augments flow interaction as well as increases heat transfer. This study may available to improve the heat generation and transfer that constitute a new epoch in fluids engineering to produce energy-related machinery.

Nomenclature

D_n : Dean number	T : Temperature
Tr : Taylor number the x -direction	u : Velocity components in the x -direction
Gr : Grashof number the y -direction	v : Velocity components in the y -direction
h : Half height of the cross section	w : Velocity components in the z -direction
d : Half width of the cross section	x : Horizontal axis
L : Radius of the curvature	y : Vertical axis
Pr : Prandtl number	z : Axis in the direction of the main flow
t : Time	λ : Resistance coefficient

Greek letters

δ : Curvature of the duct	μ : Viscosity	ν : Kinematic viscosity
ρ : Density	κ : Thermal diffusivity	ψ : Sectional stream function

Reference

- [1] Mondal RN, Kaga Y, Hyakutake T and Yanase S (2006), Effects of curvature and convective heat transfer in curved square duct flows, *Trans. ASME, Journal of Fluids Engineering*, **128**(9):1013-1022. <https://doi.org/10.1115/1.2236131>
- [2] Yanase S, Mondal RN and Kaga Y (2005), Numerical Study of Non-Isothermal Flow with Convective Heat Transfer in a Curved Rectangular Duct, *International Journal of Thermal Science*, **44**:1047-1060. <https://doi.org/10.1016/j.ijthermalsci.2005.03.013>
- [3] Rumsey CL, Gatski TB, and Morrison JH (2010), Turbulence Model Predictions of Strongly Curved Flow in a U-Duct, *AIAA Journal*, **38**(8):1394-1402. <https://doi.org/10.2514/2.1115>
- [4] Chandratilleke TT, Nadim N, Narayanaswamy R (2013), Analysis of Secondary Flow Instability and Forced Convection in Fluid Flow Through Rectangular and Elliptical Curved Ducts, *Heat Transfer Engineering*, **34**(14): 1237-1248. <https://doi.org/10.1080/01457632.2013.777249>
- [5] Ahmadloo E, Sobhanifar N, Hosseini FS (2014), Computational Fluid Dynamics Study on Water Flow in a Hollow Helical Pipe, *Open Journal of Fluid Dynamics*, **4**: 133-139. <https://doi.org/10.4236/ojfd.2014.42012>
- [6] Garnier E (2015), Flow Control by Pulsed Jet in a Curved S-Duct: A Spectral Analysis, *AIAA Journal*, 1-15. <https://doi.org/10.2514/1.J053422>
- [7] Canton J, Rinaldi E, Orlu R, Schlatter P (2019), A critical point for bifurcation cascades and featureless turbulence, *Physics.flu-dyn*, **1904.13314**.
- [8] Leong FW, Smith KA, Wang CH (2009), Secondary flow behavior in a double bifurcation, *Physics of Fluids*, **21**(043601). <https://doi.org/10.1063/1.3100211>
- [9] Sau A, Hsu TW (2007), Three-dimensional evolution of vortical structures and associated flow bifurcations in the wake of two side-by-side square cylinders, *Physics of Fluids*, **19**(084105). <https://doi.org/10.1063/1.2757712>
- [10] Lin Z, Zhu Y, Wang Z (2017), Local bifurcation of electrohydrodynamic waves on a conducting fluid, *Physics of Fluids*, **29**(032107). <https://doi.org/10.1063/1.4979064>
- [11] Machane W (2010), Bifurcation and stability analysis of laminar flow in curved ducts, *International Journal for Numerical Methods in Fluids*, **64**: 355-375. <https://doi.org/10.1002/flid.2147>
- [12] Ullah K, Ali N (2019), Stability and bifurcation analysis of stagnation/equilibrium points for peristaltic transport in a curved channel, *Physics of Fluids*, **31**(073103). <https://doi.org/10.1063/1.5097555>
- [13] Liu F, Wang L (2009), Analysis on multiplicity and stability of convective heat transfer in tightly curved rectangular ducts, *International Journal of Heat and Mass Transfer*, **52**: 5849-5866. <https://doi.org/10.1016/j.ijheatmasstransfer.2009.07.019>
- [14] Chen KT, Yarn KF, Chen HY, Tsai CC, Luo WJ, Chen CN (2017), Aspect Ratio Effect on Laminar Flow Bifurcations in a Curved Rectangular Tube Driven by Pressure Gradients, *Journal of Mechanics*, **33**(6): 831-840. <https://doi.org/10.1017/jmech.2017.93>
- [15] Yanase S, Kaga Y, Daikai R (2002), Laminar flow through a curved rectangular duct over a wide range of aspect ratio, *Fluid Dynamics Research*, **31**:151-83. [https://doi.org/10.1016/S0169-5983\(02\)00103-X](https://doi.org/10.1016/S0169-5983(02)00103-X)
- [16] Mondal RN, Kaga Y, Hyakutake T and Yanase S (2007), Bifurcation Diagram for Two-dimensional Steady Flow and Unsteady Solutions in a Curved Square Duct, *Fluid Dynamics Research*, **39**:413-446. <https://doi.org/10.1016/j.fluidyn.2006.10.001>
- [17] Nowruzzi H, Ghassemi H, Nourazar SS (2019), Linear Hydrodynamic Stability of Fluid Flow in Curved Rectangular Ducts: semi-analytical study, *Journal of Mechanics*, 1-19. <https://doi.org/10.1017/jmech.2019.5>
- [18] Lin TS, Rogers S, Tseluiko D, Thiele U (2016), Bifurcation analysis of the behavior of partially wetting liquids on a rotating cylinder, *Physics of Fluids*, **28**(082102). <https://doi.org/10.1063/1.4959890>
- [19] Nazeer G, Islam S, Shigri SH, Saeed S (2019), Numerical investigation of different flow regimes for multiple staggered rows, *AIP Advances*, **9**(035247). <https://doi.org/10.1063/1.5091668>
- [20] Zhang J, Chen H, Zhou B, Wang X (2019), Flow around an

- array of four equispaced square cylinders, *Applied Ocean Research*, **89**: 237-250. <https://doi.org/10.1016/j.apor.2019.05.019>
- [21] Hashemi A, Fischer PF, Loth F (2018), Direct numerical simulation of transitional flow in a finite length curved pipe, *Journal of Turbulence*, **19(8)**: 664-682. <https://doi.org/10.1080/14685248.2018.1497293>
- [22] Yanase S, Watanabe T, Hyakutake T (2008), Traveling-wave solutions of the flow in a curved-square duct, *Physics of Fluids*, **20(124101)**. <https://doi.org/10.1063/1.3029703>
- [23] Krishna CV, Gundiah N, Arakeri JH (2017), Separations and secondary structures due to unsteady flow in a curved pipe, *Journal of Fluid Mechanics*, **815**: 26-59. <https://doi.org/10.1017/jfm.2017.7>
- [24] Zhang W, Wei Y, Dou HS, Zhu Z (2018), Transient behaviors of mixed convection in a square enclosure with an inner impulsively rotating circular cylinder, *International Communications in Heat and Mass Transfer*, **98**: 143-154. <https://doi.org/10.1016/j.icheatmasstransfer.2018.08.016>
- [25] Wang L, Yang T (2005), Periodic oscillation in curved duct flows, *Physica D*, **200**: 296-302. <https://doi.org/10.1016/j.physd.2004.11.003>
- [26] Arpino F, Cortellessa G, Mauro A (2015), Transient Thermal Analysis of Natural Convection in Porous and Partially Porous Cavities, *Numerical Heat Transfer, Part A: Applications*, **67(6)**: 605-631. <https://doi.org/10.1080/10407782.2014.949133>
- [27] Mondal RN, Islam MS, Uddin K, Hossain MA (2013), Effects of aspect ratio on unsteady solutions through curved duct flow, *Applied Mathematics and Mechanics*, **34(9)**: 1107-1122. <https://doi.org/10.1007/s10483-013-1731-8>
- [28] Hasan MS, Mondal RN, Lorenzini G (2019), Numerical Prediction of Non-isothermal Flow with Convective Heat Transfer through a Rotating Curved Square Channel with Bottom Wall Heating and Cooling from the Ceiling, *International Journal of Heat and Technology*, **37(3)**: 710-726. <https://doi.org/10.18280/ijht.370307>
- [29] Islam MZ, Mondal RN, Rashidi MM (2017), Dean-Taylor Flow with Convective Heat Transfer through a Coiled Duct, *Computers and Fluids*, **149**: 141-155. <https://doi.org/10.1016/j.compfluid.2017.03.001>
- [30] Dean WR (1927), Note on the motion of fluid in a curved pipe, *Philos Mag*, **4**: 208-23. <https://doi.org/10.1080/14786440708564324>
- [31] Ozaki K, Maekawa H (2004), Curvature Effects in the Curved Duct for the Compressible Viscous Flow, *24th International Congress of the Aeronautical Sciences*, 1787-1792. <https://doi.org/10.1115/FEDSM2003-45634>
- [32] Chandratilleke TT, Nadim N, Narayanaswamy R (2012), Vortex structure-based analysis of laminar flow behaviour and thermal characteristics in curved ducts, *International Journal of Thermal Sciences*, **59**: 75-86. <https://doi.org/10.1016/j.ijthermalsci.2012.04.014>
- [33] Alam MM, Ota M, Ferdows M, Islam MN, Wahiduzzaman M, Yamamoto K (2007), Flow through a rotating helical pipe with a wide range of the Dean number, *Arch. Mech.*, **59 (6)**: 501-517.
- [34] Bouzit F, Laidoudi H, Blissag, Bouzit B, Ghenaim A (2018), Numerical Investigation of Power-Law Fluid Flows and Heat Transfer Inside of Curved Duct under Aiding Thermal Buoyancy, *Diffusion Foundations*, **16**: 84-95. <https://doi.org/10.4028/www.scientific.net/DF.16.84>
- [35] Bayat P, Rezaei P (2017), Semi-Empirical Estimation of Dean Flow Velocity in Curved Microchannels, *Scientific Reports*, **7(13655)**. <https://doi.org/10.1038/s41598-017-13090-z>
- [36] Li Y, Wang X, Yuan S, Tan SK (2016), Flow development in curved rectangular ducts with continuously varying curvature, *Experimental Thermal and Fluid Science*, **75**: 1-15. <https://doi.org/10.1016/j.expthermflusci.2016.01.012>
- [37] Razavi SE, Soltanipour H, Choupania P (2015), Second Law Analysis of Laminar Forced Convection in a Rotating Curved Duct, *Thermal Science*, **19(1)**: 95-107. <https://doi.org/10.2298/tsci120606034r>
- [38] Watanabe T, Yanase S (2013), Bifurcation Study of Three-Dimensional Solutions of the Curved Square-Duct Flow, *Journal of the Physical Society of Japan*, **82(074402)**: 1-9. <https://doi.org/10.7566/JPSJ.82.074402>
- [39] Harding B (2019), A Rayleigh-Ritz Method for Navier-Stokes Flow through Curved Ducts, *ANZIAM Journal*, **61**: 1-22. <https://doi.org/10.1017/S1446181118000287>
- [40] Nowruzi H, Ghassemi H, Nourazar SS (2019), Study of the effects of aspect ratio on hydrodynamic stability in curved rectangular ducts using energy gradient method, *Engineering Science and Technology, an International Journal*. <https://doi.org/10.1016/j.jestch.2019.05.004>
- [41] Norouzi M, Biglari N (2013), An analytical solution for Dean flow in curved ducts with rectangular cross section, *Physics of Fluids*, **25(053602)**. <https://doi.org/10.1063/1.4803556>
- [42] Sasmito AP, Kurnia JC, Mujumdar AS (2011), Numerical evaluation of laminar heat transfer enhancement in nanofluid flow in coiled square tubes, *Nanoscale Research Letters*, **6(376)**. <https://doi.org/10.1186/1556-276X-6-376>
- [43] Hasan MS, Mondal RN, Lorenzini G (2019), Centrifugal Instability with Convective Heat Transfer Through a Tightly Coiled Square Duct, *Mathematical Modelling of Engineering Problems*, **6(3)**: 397-408. <https://doi.org/10.18280/mmep.060311>
- [44] Jing T, He G, Li W, Zhang D, Qin F, Li R (2018), Flow and thermal analyses of supercritical hydrocarbon fuel in curved regenerative cooling channel around cavity in rocket based combined cycle engine, *Applied Thermal Engineering*, **145**: 423-434. <https://doi.org/10.1016/j.applthermaleng.2018.09.066>
- [45] Norouzi M, Kayhani MH, Nobari MRH, Demneh MK (2009), Convective Heat Transfer of Viscoelastic Flow in a Curved Duct, *World Academy of Science, Engineering and Technology International Journal of Mechanical and Mechatronics Engineering*, **3(8)**: 921-927. <https://doi.org/10.5281/zenodo.1081071>
- [46] Mondal RN, Kaga Y, Hyakutake T and Yanase S (2006), Effects of curvature and convective heat transfer in curved square duct flows, *Trans. ASME, Journal of Fluids Engineering*, **128(9)**: 1013-1022. <https://doi.org/10.1115/1.2236131>
- [47] Mondal RN, Watanabe T, Hossain MA, Yanase S (2017), Vortex-Structure and Unsteady Solutions with Convective Heat Transfer Through a Curved Duct, *Journal of Thermophysics and Heat Transfer*, **31(1)**. <https://doi.org/10.2514/1.T4913>
- [48] Ghobadi M, Muzychka YS (2015), A Review of Heat Transfer and Pressure Drop Correlations for Laminar Flow in Curved Circular Ducts, *Heat Transfer Engineering*, **37(10)**: 815-839. <https://doi.org/10.1080/01457632.2015.1089735>
- [49] Shahmardan MM, Norouzi M, Kayhani MH, Delouei AA, An exact analytical solution for convective heat transfer in rectangular ducts, *Journal of Zhejiang University -Science A (Applied Physics & Engineering)*, **13(10)**: 768-781. <https://doi.org/10.22060/MEJ.2017.12310.5311>

- [50] Gottlieb D and Orazag SA (1977), Numerical Analysis of Spectral Methods, *Society of Industrial and Applied Mathematics, Philadelphia, USA*. <https://doi.org/10.1137/1.9781611970425>
- [51] Wang L, Pang O, Cheng L (2005), Bifurcation and stability of forced convection in tightly coiled ducts: multiplicity, *Chaos, Solitons and Fractals*, **26**:337-352. <https://doi.org/10.1016/j.chaos.2004.12.026>
- [52] Yamamoto K, Wu X, Nozaki K, Hayamizu Y (2006), Visualization of Taylor–Dean flow in a curved duct of square cross-section, *Fluid Dynamics Research*, **38**: 1–18. <https://doi.org/10.1016/j.fluidyn.2005.09.002>



This document was created with the Win2PDF "print to PDF" printer available at <http://www.win2pdf.com>

This version of Win2PDF 10 is for evaluation and non-commercial use only.

This page will not be added after purchasing Win2PDF.

<http://www.win2pdf.com/purchase/>